

# The Effect of Oceanic South Atlantic Convergence Zone Episodes on Regional SST Anomalies: the Roles of Heat Fluxes and Upper-Ocean Dynamics

Luciano Ponzi Pezzi (✉ [luciano.pezzi@inpe.br](mailto:luciano.pezzi@inpe.br))

Instituto Nacional de Pesquisas Espaciais <https://orcid.org/0000-0001-6016-4320>

Mario F. L. Quadro

Federal Institute of Santa Catarina

João Lorenzetti

INPE: Instituto Nacional de Pesquisas Espaciais

Arthur J Miller

University of California San Diego Scripps Institution of Oceanography

Eliana B Rosa

INPE: Instituto Nacional de Pesquisas Espaciais

Leonardo Lima

INPE: Instituto Nacional de Pesquisas Espaciais

Ueslei A Sutil

INPE: Instituto Nacional de Pesquisas Espaciais

---

## Research Article

**Keywords:** SACZ, air-sea interaction, ocean mixed layer heat budget, ocean-atmosphere dynamic and thermodynamic, regional coupled modeling, Ekman transport.

**Posted Date:** December 29th, 2021

**DOI:** <https://doi.org/10.21203/rs.3.rs-342101/v1>

**License:** © ⓘ This work is licensed under a Creative Commons Attribution 4.0 International License.

[Read Full License](#)

---

**Version of Record:** A version of this preprint was published at Climate Dynamics on March 16th, 2022. See the published version at <https://doi.org/10.1007/s00382-022-06195-3>.

# Abstract

The South Atlantic Convergence Zone (SACZ) is an atmospheric system occurring in austral summer on the South America continent and sometimes extending over the adjacent South Atlantic. It is characterized by a persistent and very large, northwest-southeast-oriented, cloud band. Its presence over the ocean causes sea surface cooling that some past studies indicated as being produced by a decrease of incoming solar heat flux induced by the extensive cloud cover. Here we investigate ocean-atmosphere interaction processes in the Southwestern Atlantic Ocean (SWA) during SACZ oceanic episodes, as well as the resulting modulations occurring in the oceanic mixed layer and their possible feedbacks on the marine atmospheric boundary layer. Our main interests and novel results are on verifying how the oceanic SACZ acts on dynamic and thermodynamic mechanisms and contributes to the sea surface thermal balance in that region. In our oceanic SACZ episodes simulations we confirm an ocean surface cooling. Model results indicate that surface atmospheric circulation and the presence of an extensive cloud cover band over the SWA promote sea surface cooling via a combined effect of dynamic and thermodynamic mechanisms, which are of the same order of magnitude. The sea surface temperature (SST) decreases in regions underneath oceanic SACZ positions, near Southeast Brazilian coast, in the South Brazil Bight (SBB) and offshore. This cooling is the result of a complex combination of factors caused by the decrease of solar shortwave radiation reaching the sea surface and the reduction of horizontal heat advection in the Brazil Current (BC) region. The weakened southward BC and adjacent offshore region heat advection seems to be associated with the surface atmospheric circulation caused by oceanic SACZ episodes, which rotate the surface wind and strengthen cyclonic oceanic mesoscale eddy. Another singular feature found in this study is the presence of an atmospheric cyclonic vortex Southwest of the SACZ (CVSS), both at the surface and aloft at 850 hPa near 24°S and 45°W. The CVSS induces an SST decrease southwestward from the SACZ position by inducing divergent Ekman transport and consequent offshore upwelling. This shows that the dynamical effects of atmospheric surface circulation associated with the oceanic SACZ are not restricted only to the region underneath the cloud band, but that they extend southwestward where the CVSS presence supports the oceanic SACZ convective activity and concomitantly modifies the ocean dynamics. Therefore, the changes produced in the oceanic dynamics by these SACZ events may be important to many areas of scientific and applied climate research. For example, episodes of oceanic SACZ may influence the pathways of pollutants as well as fish larvae dispersion in the region.

## 1. Introduction

The South Atlantic Convergence Zone (SACZ) is an atmospheric system occurring in the warm season of South America from November to March (Casarin and Kousky, 1986; Kodama 1992; Kodama 1993; Kodama et al., 1997; Gan et al. 2009; Grimm, 2011; Quadro et al., 2012). It is characterized by marked low-level winds and a moisture convergence region that persists for at least four days (Carvalho et al. 2004; Rosa et al, 2020), and by an extensive northwest-southeast-oriented cloud band (NW-SE) (Kodama 1992, Kodama 1993). It extends from the southern center of the Amazon region, crossing the Central-West and

Southeast regions of Brazil. Its northern portion can also reach the central-south Bahia state (near 13°S and 42°W), and its southern portion as far south as the states of Paraná (near 25°S and 50°W) and Santa Catarina (near 27°S and 50°W). The SACZ can also extend towards the Southwestern Atlantic Ocean (SWA) as shown in several previous studies (Carvalho et al., 2002, Ferreira et al., 2004, Chaves and Nobre, 2004, Brasiliense et al., 2017). Figures 1a and 1b show composites of oceanic SACZ cases. Those are composites of oceanic SACZ made with outgoing longwave radiation and moisture flux divergence, based on four cases, which are studied and further discussed here.

In the regions affected by the SACZ, one of the main consequences is the occurrence of high rainfall, particularly in late austral spring and summer months (Grimm, 2011; Quadro et al. 2012). One of the main mechanisms contributing to the SACZ configurations is the so-called South American Monsoon System (SAMS), which is responsible for moisture transport from northern Brazil and the Amazon region to central and southeast South America (Casarin and Kousky, 1986; Kodama 1992, 1993; Kodama et al., 1997; Gan et al. 2009; Grimm, 2011; Quadro et al., 2012). Jorgetti et al. (2014), however, suggest that the SACZ can occur in both active and inactive phases of SAMS, resulting in different intensities and positions of the cloudiness band. The SACZ is therefore an important large-scale feature during summertime in tropical South America region (Kodama, 1992; Nougés-Paegle and Mo, 1997; Satyamurty et al., 1998; Liebmann et al. 1999).

As a result, SAMS and SACZ modulate the seasonal cycle of precipitation over tropical South America in a region between the equator and 25°S (Silva, 2009). Gan et al. (2004) showed that 50% of the annual rainfall over tropical and subtropical South America occurs in the austral summer months (Dec/Jan/Feb) and about 90% of it in the period from October to April. Marengo (2005), analyzing the temporal and spatial variability of the moisture balance in the Amazon basin and surrounding areas, showed that the spring and summer periods present a strong convergence of moisture throughout the SACZ climatological positioning. However, atmospheric blocking events occurring in subtropical South America can prevent SACZ formation (Rodrigues and Woollings, 2017; Rodrigues et al., 2019), leading to a deficient rainy season in the Central-West and Southeast regions of Brazil.

Previous studies suggest that reduced cloudiness in late spring (end of dry season) in Central-West and Southeast Brazil would eventually increase net surface solar radiation over the Southeast Brazilian coastal region and offshore Southwest Atlantic Ocean. This condition, in turn, would favor a pressure drop, increasing convergence at low levels and an anomalous atmospheric cyclonic circulation in southeastern Brazil. These characteristics, which are associated with increased convection, tend to intensify precipitation in the Central-West region of Brazil and develop atmospheric configurations that end up favoring the establishment of the SACZ (Grimm et al., 2007).

One of the first articles that mentioned the role of the "Oceanic SACZ" and its implications for precipitation was developed by Carvalho et al. (2002). They argue that ~65% of all extreme rainfall events occur when convective activity in the SACZ is spatially extensive and intense. In ~30% of cases where intense precipitation occurred north of São Paulo State, they were associated with an intense SACZ with

deep convective activity extending towards the Atlantic Ocean, suggesting that the SACZ probably played an important role in the increase of convection in southeastern Brazil. Regarding large-scale forcings, there is an intensification of convection over the Southwest Atlantic Ocean (Carvalho et al. 2002; Carvalho et al. 2004; Ferreira et al. 2004) during El Niño years and greater convection over the continent in La Niña years. Thus, some have proposed that the oceanic SACZ is sensitive to the SST in the Southwest Atlantic and consequently to the precipitation in South America (Tascheto et al. 2008). One of the patterns of variability in SST is the South Atlantic Dipole, which is characterized by the surface thermal gradient between the Tropical and South Atlantic. This influence has been verified during neutral ENSO conditions (Bombardi et al., 2014a; Bombardi et al., 2014b).

The SACZ can also occur in association with other atmospheric and oceanic phenomena, being influenced by local or remote factors (Kodama, 1992; Kodama et al., 1997; Grimm and Silva Dias, 1995; Grimm et al. 2007; Nogués-Paegle and Mo, 1997; Jones and Horel, 1990, Marton, 2000, Chaves and Nobre, 2004, Hirata and Grimm, 2015, Pezzi et al., 2016, Pezzi et al., 2021). These issues have been addressed in numerical modeling studies that simulate the SACZ in its atmospheric and oceanic components (Chaves and Satyamurty, 2006; Chaves and Nobre, 2004), as well as in reanalysis-based studies dedicated to understanding the spatial and temporal variability of the SACZ (Carvalho et al., 2004, Ferreira et al., 2004 and Grimm and Zilli, 2009). For example, atmospheric frontal systems in the region of the SACZ may interact with cyclonic sub-synoptic scale high-level vortices (Nobre, 1988). Oscillations in the period band of 30 to 60 days may create atmospheric disturbances that trigger the convection associated with the SACZ (Casarin and Kousky, 1986) and explosive convection over central and southern Amazonia, responsible for the generation of the convergence zone at low levels (Figueroa and Nobre, 1990). Robertson and Mechoso (2000) have presented observational evidence that positive (negative) SST anomalies in the Southwest Atlantic are associated with a weakening (strengthening) of the SACZ. On the other hand, experiments with atmospheric global circulation models show that precipitation in oceanic regions tends to intensify over warm waters (Barreiro et al., 2002).

It should be noted, however, that two possible cooling mechanisms of the ocean surface can be present during SACZ events; one is here referred to as thermodynamic and the other as dynamic. Both will now be discussed and are summarized in Figure 1c. Chaves and Nobre (2004) and Almeida et al. (2007) have suggested that the occurrence of a negative SST anomaly under the SACZ position is a result of negative feedback between the SACZ, cloud cover, and SST, with the atmosphere forcing the ocean. Atmospheric convection over the SWA increases the amount of clouds. These, in turn, reduce solar radiation at the ocean surface, and promote the cooling of it. Convection over cold waters tends to diminish, dissipating the oceanic portion of the SACZ. The tendency of atmospheric general circulation models (AGCM) to underestimate precipitation over cold waters in the SACZ region, as suggested by Nobre et al. (2012), is attributed to the non-active thermodynamic coupling in this class of models, which differs from ocean-atmosphere coupled models. In this way the authors proposed that the oceanic part of the SACZ is a thermally indirect circulation cell, with intense convection occurring over waters with lower SST values. This is the thermodynamic mechanism responsible for the cooling of the surface of the ocean, Figure 1c top panel.

In addition to the aforementioned thermodynamic process, Kalnay et al. (1986) suggested that in one SACZ case the atmosphere forced negative SST anomalies in the Southwestern Atlantic Ocean via low level cyclonic vorticity, which induces upward flow in the underlying ocean (Ekman pumping), bringing colder subsurface waters to the surface layer (upwelling). At the same time, the SACZ-cloud-SST feedback intensifies the negative SST anomaly. The cyclonic circulation tends to cease over colder waters due to the Marine Atmospheric Boundary Layer (MABL) vertical mixing adjustment to SST. Over colder waters, air buoyancy and turbulence are reduced, increasing the vertical wind shear (Wallace et al., 1989; Pezzi et al. 2005). The same dynamic feedback of SACZ-Ekman pumping-SST is mentioned in Chaves and Nobre (2004), analyzing December, January, and February averaged SST fields. They found, however, that this dynamic mechanism was one order of magnitude weaker than the thermodynamic one. Up to now, from what is known, the thermodynamic mechanism has been taken as the major mechanism responsible for the oceanic surface cooling (Figure 1b, lower panel). Our study will challenge this idea by reanalyzing in more detail the dynamic mechanism as further discussed in our results and conclusions section.

An important sector of the SE Brazilian coast is the South Brazil Bight (SBB), a highly productive semi-enclosed marine ecosystem extending from Cabo Frio (23°S, Rio de Janeiro State, RJ) to Cabo de Santa Marta (28°40'S, Santa Catarina State, SC), where intense fishing activity is concentrated. Its location can be seen in the studies of Castro (2014) and Soares et al (2011), and in Figure 1. This is a region encompassing four Brazilian states and a population of about 82 million people. Despite its importance, the SACZ atmospheric effects on the cooling of this Southwest Atlantic region, and associated impact on regional climate and marine ecosystems, has not yet been given due attention. The SBB has a strong seasonal cycle in its physical oceanography - SST, vertical stratification, thermal and haline fronts, upwelling plumes, and currents (Castro, 2014; Cerda and Castro, 2014), and its biological and fishery productivity (Soares et al., 2011; Dias et al., 2014, D'Agostine et al., 2015; Endo et al., 2019). This oceanic seasonality seems to be highly associated with the atmospheric seasonality (Castro and Miranda, 1998). The most important atmospheric system affecting SBB seasonality is the South Atlantic Subtropical High (SASH), the large-scale semi-permanent pressure center that influences the wind patterns on the Brazilian coast and causes the predominantly northeast wind direction in the SBB in summer (Pezzi and Souza, 2009b). Some studies indicate a relationship between the sardine biological cycle and fisheries of SBB to the oceanic and atmospheric physical variability (Matsuura, 1998; Sunyé and Servian, 1998; Cergole et al., 2002; Gigliotti et al., 2010; Soares et al., 2011; Dias et al., 2014, D'Agostine et al., 2015; Endo et al., 2019). These results show the important connection between ocean-atmosphere interactions and the SACZ with the ecosystem dynamics of the ocean in the region.

With the above context in mind, our main objective in this study is to investigate the coupling between the atmosphere and the SWA surface layer waters in terms of air-sea interaction processes. We achieve this by using a coupled ocean-atmosphere model to simulate oceanic SACZ episodes (i.e., with strong convective activity over its oceanic portion) selected from the study made by Rosa et al. (2020). Our main interests and novel results are on verifying how the SACZ influences both dynamic and thermodynamic

mechanisms in the oceanic mixed layer (OML) that contribute to the sea surface thermal balance in that region, through changes in the OML velocity field and surface net heat fluxes, respectively.

We organize the article as follows: Section 2 introduces the regional numerical coupled system used to simulate four intense oceanic SACZ episodes. In Section 3 we present a broad overview of the simulated cases and compare three different model setups: (i) atmospheric model with prescribed SST, (ii) oceanic and atmospheric coupled and (iii) oceanic, atmospheric and wave models all actively coupled. Section 4 analyses the dynamic mechanism for the whole set of cases, while Section 5 presents a mixed layer heat budget analysis for the SWA. The article finishes with conclusions and final remarks in Section 6.

## 2. Methods And Data

### 2.1 The regional coupled system

In this section we present the Coupled Ocean–Atmosphere–Wave–Sediment Transport (COAWST) Modeling System v 3.2 (Warner et al., 2010). This modeling system combines three well known numerical models: (i) the atmospheric model is the Weather Research and Forecasting Model v 3.7.1 (WRF) (Skamarock et al., 2005); (ii) the Regional Ocean Modeling System svn 797 (ROMS) (Shchepetkin and McWilliams, 2003, 2005; Haidvogel et al, 2008) is the hydrodynamic ocean model; (iii) the wave model is the Simulating Waves Nearshore (SWAN) v 41.01AB (Booij et al., 1999); plus a sediment transport model named Community Sediment Transport Modeling Project (CSTM) (Warner et al., 2008). All these models can be actively coupled, but for the purposes of this study CSTM is not used. The coupling is performed using the Model Coupling Toolkit v 2.6.0 (MCT, Larson et al. 2005, Jacob et al. 2005). COAWST is an open-source system that is based on individual open-source models (Warner et al., 2010). Pullen et al. (2018) present an interesting review about coupled modeling frameworks where some of the ocean-atmosphere interaction cases were modeled to investigate and forecast the coupling between tropical cyclones and the ocean, such as the hybrid and first registered hurricane in the South Atlantic, the Catarina event (McTaggart-Cowan et al., 2006).

COAWST is a modular system that allows an active coupling between the ocean and the atmosphere, where the fluxes are actively traded in both directions, from the atmosphere to the ocean and vice versa. It has allowed advances in the representation of coastal dynamics due to the coupling of oceanic and atmospheric circulation models and waves and sediment transport models (Lesser et al, 2004; Warner et al, 2008). This system allows the regional simulation of thermodynamic and dynamic large-scale systems for both atmospheric (Miller et al. 2017; Pullen et al., 2018) and oceanic phenomena (Mendonça et al., 2017). When regionalized, this system can produce simulations in greater detail, allowing the assessment of their effects on regional scales (Mendonça et al., 2017). Each of the system components has been developed and applied to idealized and realistic scenarios. Some of the ocean-atmosphere applications were made to investigate and forecast the interactions between tropical cyclones and the ocean (Bender and Ginis, 2000; Bender et al, 2007; Chen et al, 2007; Warner et al. 2010; Mendonça et al., 2017; Miller et al. 2017; Pullen et al. 2018).

The run of each model begins from its own initial and boundary conditions. After a number of user selected time steps, the models reach a synchronization point. From this point on, the flux exchanges between ocean and atmosphere occur via a Model Coupling Toolkit (MCT) scheme that sends and receives data between the coupled models. Since each model may have a different grid, there is a pre-processing in which the interpolation weights are calculated for each model grid through the remapping Spherical Coordinate Interpolation Package - SCRIP (Jones, 1998). Sutil and Pezzi (2020) provide a very detailed description of each model that makes up the COAWST and bring a detailed explanation on how to generate the numerical grids of the models as well as the generation of initial conditions, boundary conditions of each model component. In addition, they show how to install and run COAWST on a personal computer.

## 2.2 Models and experimental design

The ROMS is a 3-D oceanic regional model that has a free surface with terrain following vertical sigma coordinates. For the present study, it was configured with a horizontal grid domain ranging from 55°S to 5°S and 70°W to 20°W, to represent the SWA region. The horizontal resolution is 1/12° (approximately ranging from 9.2 km to 6 km) and a vertical discretization of 30 sigma levels, with 40s and 90s for barotropic and baroclinic time-steps, respectively. The surface and bottom stretching parameters are 5 and 0.6, respectively, with a 50m critical depth controlling the stretching and default vertical coordinate transformation. It solves the Navier–Stokes equations by using Reynolds averaging, Boussinesq approximation and hydrostatic vertical momentum balance (Shchepetkin and McWilliams, 2005). The model has been widely used for many applications such as ocean circulation forecast (Haidvogel et al. 2008), biophysical modeling (Dias et al., 2014, D’Agostini et al., 2015), biogeochemical modeling (Arruda et al., 2015), air-sea interaction studies (Putrasahan et al., 2013a, Putrasahan et al., 2013b; Seo et al., 2007; Seo, 2017; Miller et al., 2017; Pullen et al., 2018) and South Atlantic coastal studies (Mendonça et al. 2017; Combes and Matano 2014; Palma et al. 2008). In the following, the main physical parameterization options used for ROMS are listed. For momentum, horizontal harmonic viscosity is used (Wajsowicz, 1993); for tracers equations, a 3rd-order upstream horizontal advection is invoked (Shchepetkin and McWilliams, 2005); the pressure gradient algorithm uses a spline Jacobian density (Shchepetkin and McWilliams, 2003); the wave roughness formulation uses a Taylor and Yelland relation (Taylor and Yelland, 2001); horizontal mixing of momentum is calculated using constant sigma surfaces (Shchepetkin and McWilliams, 2003); horizontal mixing of tracers is determined on geopotential (constant depth) surfaces (Shchepetkin and McWilliams, 2003) and for vertical mixing of momentum and tracers a generic length-scale formulation is used (Warner et al., 2004).

The WRF model provides all surface atmospheric fields to the ocean model, such as long and shortwave radiation surface fluxes, precipitation, atmospheric pressure, relative humidity, air surface temperature, and wind velocity at 10 m. It was configured to match the same oceanic domain with horizontal resolution slightly finer than the oceanic, 6 km, approximately. The model also uses terrain-following vertical-sigma coordinates with 45 levels. The physical parameterization schemes chosen for this study were also used in previous studies such as in Shi et al. (2010), Tao et al. (2011) and Nicholls and Decker

(2015). The microphysics scheme is Goddard (Lang et al. 2007); the cumulus convection is Kain-Fritsch (Kain, 2004); the longwave and shortwave radiation schemes are the new Goddard scheme (Chou and Suarez, 1999); the surface layer is the Eta similarity (Monin and Obukhov, 1954); the atmospheric boundary layer is Mellor-Yamada-Janjić (Mellor and Yamada, 1982; Janjić, 2002) and the land surface scheme is Noah (Chen and Dudhia, 2001).

The oceanic open boundaries (north, east, and south) were forced using temperature, salinity, current velocities, and sea surface height 5-day means obtained from Simple Ocean Data Assimilation v 3.3.1 (SODA) (Carton and Giese, 2008). The National Centers for Environmental Prediction (NCEP) Final Operational Global Analysis (FNL) provided the atmospheric lateral boundaries. The prescribed SST used on WRF uncoupled experiments is from the Real Time Global (RTG) analyses developed at NCEP of the National Oceanic and Atmospheric Administration (NOAA) for use in weather prediction and modeling, particularly at high spatial resolution and short time range. The version used here has 0.5 degree of horizontal resolution and daily temporal resolution.

The selected cases for the study of the oceanic SACZ and the periods of numerical integration are based on the work of Rosa (2017) and Rosa et. al (2020), in which an automatic classification algorithm was developed and used. It is based on some parameters, such as cloud cover band defined by OLR values lower than  $230 \text{ W m}^{-2}$ , and the life cycle and positioning over the SACZ region. From this information the method classifies the SACZ as continental or oceanic and of the oceanic cases we selected four of them based on their well-defined oceanic configurations. The numerical experiments were carried out for two periods. The first goes from December 1st, 2002 to January 31st, 2003. The second was from December 1st to 31st, 2013. The four oceanic SACZ analyzed episodes were extracted from those two integration periods, as shown in Table 1. The atmospheric and oceanic models were initialized at the beginning of those periods from SODA and NCEP FNL, respectively. The investigation started by verifying if the model setups were able to reproduce the observed oceanic SACZ episodes. This was accomplished by integrating WRF in uncoupled mode for both periods described above, and this experiment was named WRF, as shown in Table 1. Experiments named COA, are for the two-way coupled model configuration, using WRF and ROMS; experiments named COA2 uses WRF, ROMS and SWAM, also shown in Table 1. The idea of simulating four cases of oceanic SACZ using three model (multi-model) configurations was to increase the number and variety of experiments that could reduce uncertainties in the oceanic SACZ simulations. That is, a more robust ensemble of results is obtained with simulations performed with different COAWST setups. It should also be noted here that it is not in the scope of this work to analyze and compare the pros and cons of each COAWST setup. Instead, it was to obtain atmospheric and oceanic simulations that would allow a dynamic and thermodynamic analysis, as shown below.

Table 1

– Name of experiment, period of SACZ episode, model setup, and SACZ episode characteristic (SACZ Oceanic=yes, SACZ Continental=no).

Experiment	Period	Model	Oceanic SACZ
1_WRF	10/12/2002 to 16/12/2002	WRF	yes
1_COA	10/12/2002 to 16/12/2002	WRF ROMS	yes
1_COA2	10/12/2002 to 16/12/2002	WRF ROMS SWAN	yes
2_WRF	13/01/2003 to 19/01/2003	WRF	yes
2_COA	13/01/2003 to 19/01/2003	WRF ROMS	yes
2_COA2	13/01/2003 to 19/01/2003	WRF ROMS SWAN	yes
3_WRF	25/01/2003 to 31/01/2003	WRF	yes
3_COA	25/01/2003 a 31/01/2003	WRF ROMS	yes
3_COA2	25/01/2003 to 31/01/2003	WRF ROMS SWAN	yes
4_WRF	10/12/2013 to 24/12/2013	WRF	yes
4_COA	10/12/2013 to 24/12/2013	WRF ROMS	yes
4_COA2	10/12/2013 to 24/12/2013	WRF ROMS SWAN	yes
5_WRF	27/12/2002 to 07/01/2003	WRF	no

Experiment	Period	Model	Oceanic SACZ
5_COA	27/12/2002 to 07/01/2003	WRF	no
		ROMS	
5_COA2	27/12/2002 to 07/01/2003	WRF	no
		ROMS	
		SWAN	

## 2.3 Auxiliary data

The auxiliary satellite data were used mostly to verify if the model was satisfactorily simulating the oceanic SACZ episodes. The objective of this analysis was to visually compare the fields generated by the simulation against satellite-derived ones, not for quantifying or evaluating the model biases and errors or even stating which model setup or physical parameterizations best suits the oceanic SACZ simulations. The satellite measurements of Outgoing Longwave Radiation (OLR) and precipitation used here were retrieved from the NOAA Daily OLR and Global Satellite Mapping of Precipitation (GSMaP). The OLR is a data set retrieved from twice daily Advanced Very High-Resolution Radiometer (AVHRR) data. This data set is available as daily values from January 1st, 2002 to the present, 2.5° latitude x 2.5° longitude global grid. The GSMaP, version MVK (GSMaP\_MVK) is a set of new high-resolution precipitation estimates based on blending passive microwave (PMW) sensors and infrared (IR) radiometers data to produce estimates of rainfall over the globe at a spatial resolution of 0.1° latitude/longitude and hourly temporal resolution (Ushio et al., 2009). As remarked by many investigators, satellite data supply crucial information where *in situ* data are very sparse or nonexistent, which is the case over the Southwest Atlantic (the major focus of this work) and over some parts of the continent.

## 3. Main Features From Oceanic Sacz Simulations

In this section, the main results obtained by the set of oceanic SACZ simulations are presented. First, we analyze and show that our set of simulations can reproduce the expected oceanic SACZ effect on SST. Next, their spatial features are compared against satellite data. Finally, an analysis is performed to evaluate the simulated oceanic SACZ dynamics at SWA.

### 3.1 SST time series

As discussed above, during active oceanic SACZ episodes, SST values are expected to decrease in the SWA region affected by the atmospheric convergence. This result was observed in all simulated oceanic SACZ episodes, as displayed in Figure 2. Figure 2a shows the simulation from 1 December 1st 2002 to January 31st 2003 while Figure 2b from December 1st 2013 to December 31st 2013 (see Table 1 for the experiment names and more detail). The time series are the SST area averaged over the SWA that is under the SACZ's influence, here defined as the region from 20° to 33°S to and from 35° to 45°W. WRF

curves are presented only as a reference since they were not simulated but used as prescribed SST bottom boundary conditions for the atmospheric model. As indicated in the figure, SST values indeed tend to decrease during the SACZ episodes as shown in the area averaged four selected cases (Figure 2a and 2b). This is clearly observed for the fully active coupled model runs, COA and COA2. For both observed and simulated SSTs, we see that atmospheric conditions associated with the SACZ, particularly the surface winds and cloud cover, act to modify the oceanic surface thermal condition. An opposite situation that has attracted a great deal of attention is seen in case 5 (Table 1 and Figure 2a) where the SST increases. This is, however, a case where the SACZ is concentrated over the continent (not shown), thus not strongly affecting either the solar radiation reaching the ocean's surface, nor the atmospheric dynamics over the ocean. This is a case of continental SACZ, which is out of the scope of this study.

## 3.2 SACZ spatial features

In order to analyze the spatial characteristics of the simulated set of oceanic SACZ episodes, at each model grid point a time mean of the four cases was calculated based on the dates of the cases shown in Table 1 (Figures 3 and 4). To show that distinct model configurations can simulate oceanic SACZ episodes in a reasonable way it is necessary to compare simulated precipitation and outgoing longwave radiation (OLR) with observed ones. This comparison assures us that the model is simulating cases of oceanic SACZ. However, the purpose here is qualitative similarity, not to quantitatively evaluate model bias or deeply investigate the impacts of each specific model setup on the SACZ simulation.

All spatial observed and simulated results presented hereafter were calculated as the mean of the four oceanic SACZ simulated cases, based on the dates of the cases shown in Table 1. Figure 3 shows clearly for the three models the northwest/southeast oriented higher values of precipitation band. In some regions, modelled precipitation reaches 55 to 60 mm.day<sup>-1</sup>, Figure 3a to 3c. Note that the WRF simulation shows a larger area with higher precipitation over the oceanic region; this might be associated with the prescribed bottom boundary conditions over the ocean SST values, which are higher for this simulation (Figure 5b) compared to the other two simulations made with the fully coupled models, COA and COA2 (Figure 5e and 5h). A maximum precipitation of that magnitude is not, however, seen in the observed satellite data (Figure 3d).

The SACZ cloud band position and intensity can be inferred from lower values of OLR (Figure 4). OLR lower values (a proxy of cloud cover presence) are observed over the oceanic region (as well as over the adjacent continental region). The different model runs were able to simulate reasonably well the SACZ episodes, especially when compared with satellite derived OLR and cloudiness estimated from infrared satellite images (not shown here). Like what was observed for precipitation, the WRF experiment simulates a less intense OLR belt compared to the other two experiments. However, satellite-derived minimum values of OLR (Figure 4d) show a larger extension, indicating a larger area of stronger convection as compared to simulation.

Considering simulated precipitation and OLR (generated under different model setups) and observation, it is fair to say that numerical simulations reproduce reasonably well the oceanic SACZ episodes features.

Therefore, we can consider the model results a good proxy data set for the study of oceanic SACZ episodes, even considering the bias seen on precipitation and OLR. We also highlight that our main interest is in detecting the mechanisms through which the OML is modified by oceanic SACZ, not necessarily the absolute magnitude of each dynamic or thermodynamic term of the heat balance.

### 3.3 Dynamic aspects and tendency analysis

Here, we will first analyze the sea level pressure (SLP) and associated surface wind field at 10 m height during oceanic SACZ (Figures 5a, 5d and 5g). The western branch of the South Atlantic Subtropical High (SASH) is indicated in these figures by the E and ENE winds. The SASH is the semi-permanent high-pressure system that is predominant over this region, which migrates northwards (southwards) during austral winter (summer) (Pezzi et al. 2009b). Note that because of the SASH, the surface winds are upwelling favorable, flowing southwards and almost parallel to the coast in the region from 21°S to 15°S.

However, the most remarkable pattern observed in these results is a surface low pressure cyclonic vortex centered at 24°S and 43°W (approximately) on the Southwestern Atlantic Ocean which appears at the surface (Figure 5a, 5d and 5g) and higher levels, such as on 850 hPa (Figure 5c, 5f and 5i). It encompasses all the Southern Brazilian Continental Shelf (SBCS) and offshore oceanic region, being centered in the southern edge of the oceanic SACZ. This striking feature is consistently seen in the three model experiments. A very similar feature is presented by Brasiliense et al. (2017) in their analysis of a specific case of oceanic SACZ and in Rosa et al. (2020) for the composite of all oceanic SACZ cases found by the authors. Following Rosa et al. (2020) we designate this feature as the cyclonic vortex Southwest of oceanic SACZ (CVSS). Both effects, the SASH surface high pressure atmospheric circulation and resulting Cabo Frio upwelling, together with the offshore SBCS upwelling caused by CVSS, are discussed in the following section.

The SST time tendency ( $SST_{tend}$ ) was estimated by subtracting from the average SST, calculated for the days of active oceanic SACZ ( $\overline{SST_{episodes}}$ ), the average temperature of the day before the beginning of each individual SACZ episode ( $SST_{d-1}$ ).

$$SST_{tend} = \overline{SST_{episodes}} - SST_{d-1} \quad (1)$$

SST tendency superimposed on OLR is presented in Figures 5b, 5e and 5h. These OLR fields are slightly different from those in Figure 4; here we display only OLR values lower than  $250 \text{ Wm}^{-2}$ , a threshold chosen to isolate the convection. With this threshold, it is possible to better identify areas where convection associated with the SACZ is well organized, active, and possibly affecting the surface waters. The surface cooling produced by SACZ episodes is well characterized in all experiments (blue colors). Note first that the oceanic model with a higher spatial resolution of about 6 km (COA in Figure 5e and COA 2 in Figure 5h) produces an SST field with much more details as compared to the prescribed lower resolution SST field used in the WRF simulation. When compared to the observed prescribed SST for the WRF experiment, the COA and COA2 model show a stronger cooling that is not restricted to the region

right underneath the SACZ cloud band. Interestingly, this cooling extends further south from the southern edge of the SACZ, reaching the SBCS region and extending very far offshore.

Moisture flux divergence and the associated vector wind field at 850 hPa during the SACZ episodes are displayed in Figure 5c, 5f and 5i. As indicated by the negative values (blue colors), a convergence of moisture flux is present throughout the oceanic SACZ (850 hPa) region. The shape of the moisture flux divergence field over the ocean (simulated by all experiments) follows a typical oceanic SACZ pattern, where it occurs southwest of the SASH. The humidity transport is the main mechanism responsible for the SACZ precipitation over the ocean and further west over the continent. The CVSS presence during oceanic SACZ has been previously identified (Rosa, 2017; Brasiliense et al., 2017; Rosa et al. 2020). In cases of continental SACZ this system is seen as a trough, while in oceanic episodes it appears as a closed cyclonic vortex (Quadro et al. 2016, Rosa et al. 2020). Right underneath the cyclonic vortex circulation a large area of sea surface cooling as well as a decreased humidity is observed, as indicated by the positive moisture flux divergence (red colors).

### 3.4 Oceanic SACZ impacts in OML's dynamics and tendency analysis

In this section, we investigate the coastal and offshore upwelling processes during oceanic SACZ episodes and the associated impact on the SST. Several studies have analyzed SST tendencies associated with oceanic vertical velocity and Ekman pumping dynamics, such as Small et al. (2015) for the Benguela upwelling system, and Seo et al. (2012) for the California Current system. The so-called Cabo Frio upwelling system, located at SBB, is a wind forced coastal upwelling, which has also been extensively studied. Rodrigues and Lorenzetti (2001) showed via numerical modelling the impact of the continental shelf bottom topography and coastline geometry in controlling the position and intensity of upwelling plumes in the region. Castelão et al. (2006) showed that upwelling favorable negative wind stress curl prevails throughout the year, but is intensified during the summer, when the wind blows for several consecutive days from the NE direction, affecting the SST seasonality.

Here we analyze, via the linear Ekman pumping vertical velocity ( $w_E$ ), the importance of the wind stress curl to the upwelling in the SBCS and adjacent offshore region under oceanic SACZ atmospheric dynamic influence.

$$w_E = \frac{\nabla \times \vec{\tau}}{\rho f} \cdot \vec{k}$$

2

where  $\vec{\tau}$  is the wind stress,  $\vec{k}$  is the unit vector in the vertical direction,  $\rho$  is the seawater density and  $f$  is the Coriolis parameter. The surface wind stress and its spatial and temporal variability is the main atmospheric forcing of the ocean circulation (the wind-driven component) in the near surface oceanic frictional (turbulent) layer but affecting the ocean interior via mass convergences and divergences in that

layer (Talley et al. 2011). These are the main dynamical mechanisms connecting the surface turbulent atmospheric layer to the ocean interior. For the southern hemisphere ( $f < 0$ ), the negative wind stress curl is the physical mechanism responsible for the positive surface oceanic divergence that in turn induces upward motion in the Ekman layer, bringing deeper and colder waters to the surface layer. On the other hand, positive wind stress curl causes surface convergence, inducing downward water movement.

Coastal upwelling in the SH is normally associated with an along shore wind field blowing predominantly from a direction having the coastline to its right. This induces an offshore surface Ekman flow, a positive divergence on the coast, and a positive vertical flow (upwelling). In this case, the cooling effect on SST will only be effective if cold bottom waters are present near the coast, which is the case in the region during the spring and summer seasons. Note that the coastal upwelling can occur even for a vorticity free wind flow, but a combination of coastal flow divergence with a negative vorticity large scale wind can result in a strengthened regional upwelling.

Related to the effect of Ekman pumping on SST variability in the region, we divided the analysis in two parts, the SBCS continental shelf upwelling system, and the offshore deep ocean upwelling. For the sake of brevity, here we show only the results of COA2 simulations, since WRF and COA (mainly) did not significantly diverge on their results from those found with COA2. Additionally, the COA2 experiment shows the lowest bias for precipitation and OLR as compared with satellite observations (Figures 3 and 4).

Large areas of negative wind stress curl of up to  $-1.0 \times 10^{-6} \text{ Nm}^{-3}$  are seen over the coastal SBCS from  $17^\circ\text{S}$  to  $23^\circ\text{S}$ , including the Cabo Frio coastal upwelling system region (Figure 6a). Over this coastal region a relatively strong, along shore, southward blowing, and upwelling favorable, wind stress is observed (Figure 6a). As indicated in the figure, this alongshore wind field has a strong negative vorticity, associated with an offshore intensification of this negative wind stress. The vorticity of the wind produces an Ekman pumping and an average upwelling flow ( $w_E$ ), given by Eq. 2, of up to  $1.5 \text{ m day}^{-1}$  (Figure 6b) in that area. The total oceanic vertical velocity at 40 m depth (typical mixed layer depth) as given by the ROMS simulation ( $w_{ROMS}$ ) is shown in Figure 6c, with horizontal currents superimposed on it.  $w_{ROMS}$  has a similar spatial structure to the Ekman pumping field (Figure 6b) but shows stronger upward vertical velocities of up to  $2.5 \text{ m day}^{-1}$ . These higher vertical velocities are likely being produced by a joint effect of wind vorticity, coastal upwelling, and bottom topography-forced vertical flow (mostly in the shelf/slope region). The similarity of  $w_E$  and  $w_{ROMS}$  fields shows that the atmospheric component alone (the curl of the wind stress) as seen in the  $w_E$  results is highly important, but from the oceanic side the vertical velocities, as modeled by  $w_{ROMS}$ , contain additional dynamic factors that regionally modulate and strengthen the  $w_E$  flow.

On the southern portion of the SBCS, between  $23^\circ\text{S}$  and  $28^\circ\text{S}$  (Figure 6), there is a large offshore area of negative wind stress curl, oriented in the northwest/southeast direction. This is well aligned with the oceanic SACZ, but shifted southward (Figure 6a), as can be seen comparing it with the SACZ convection

belt, inferred from OLR in Figure 5h. This large negative wind stress curl area is associated with a large area of positive vertical Ekman velocities (Figure 6b). They are not as intense as those seen near the coast, although they still produce considerable upwelling, with vertical velocities ranging from 0.7 to 1.0 m day<sup>-1</sup>. This region is under atmospheric influence of the surface low-pressure system, the CVSS, as derived from the set of simulations (Figure 5a, 5d and 5g), which is producing a cyclonic wind stress circulation and upward water movement seen in  $w_E$  and in the vertical velocity simulated by the ocean model Figure 6c.

The presence of the Brazil Current (BC), the western boundary current of the South Atlantic, can be clearly seen in the surface current field generated by COA2 (Fig. 6c). This southward flow is present throughout the year in the region, normally being present offshore of the outer shelf and shelf break regions. It transports warm and saline tropical waters (Legeckis and Gordon, 1982; Lima et al., 1996; Assireu et al., 2003; Souza and Robinson, 2004, Goes et al. 2019), and flows to the south up to about 40°S where it meets the colder and fresher northward flowing Malvinas Current (MC). The region where these two currents collide is called the Brazil Malvinas Confluence (BMC). Strong modulations in MABL stability have been documented in the frontal zone separating warm BC from cold MC waters (Pezzi et al., 2005, 2009a) and by warm core eddy at the Atlantic Southwest (Pezzi et al. 2021). Another interesting feature seen in the simulated oceanic near-surface currents is a train of cyclonic eddies extending in the same direction and region of the negative wind stress curl areas. Here we highlight three of them with their centers located at 26°S and 42°W, 27.5°S and 33°W, 28°S and 27°W, approximately (marked as A, B, and C in Fig. 6c). This is a deep oceanic region and therefore without the influence of complex topography, but a number of oceanic eddies are frequently seen in the region. Similar eddies in this region have already been reported (e.g. Calil et al. 2021). The largest cyclonic eddy (26°S and 42°W) is right underneath the CVSS and it is possible that its intensity can be affected by this specific atmospheric phenomenon. An upper ocean vertical section at 26°S (not shown) shows a shoaling thermocline near the shelf slope and decreased temperature between 44°W to 42°W, approximately the region of the core of the cyclonic eddy “A” is, as shown in Figure 6c. Cyclonic eddies also generate upward movement in their cores; values ranging from 0.6 m day<sup>-1</sup> to 2.5 m day<sup>-1</sup> are seen associated with these features. Therefore, we can say that under the presence of the oceanic SACZ, Ekman pumping (negative wind curl) and cyclonic eddies may play a joint (near coast), or separate (offshore), significant role in lowering the heat content of surface waters. That is, both Ekman pumping and eddy dynamics might be in effect in the cooling of surface waters of the region.

In order to complement this analysis, we superpose the horizontal net current effects and wind stress on SST (each as tendencies following Eq 1) as shown in Figures 6d and 6e. However, here we used the 3-day averages before the SACZ episodes on the last term on the r.h.s. of Equation 1. Figure 6e (currents during SACZ minus previous three days) reveals that during SACZ episodes the difference currents are from the south, meaning that all southward flow, including the Brazil Current, is weakened. It is possible to see that within the entire negative area of SST there is a predominance of anomalously weaker circulation from the north, as indicated by the northwards-oriented current vectors (Figure 6e).

This modulation analysis of the oceanic currents is complemented by the volume transport calculations over the area shown in Figure S1, supplementary material. We performed this calculation over three distinct latitudes (22 to 26°S) within our interest area and for three distinct periods. However here we focus our analysis at 26°S right over the oceanic cyclonic eddy seen also in Figure 6c. The results obtained from the area in Figure S1, show that the volume transport is -11.15 Sv (1 Sv = 10<sup>6</sup> m<sup>3</sup>.s<sup>-1</sup>) for all cases of oceanic SACZ (Figure S1a), meaning that the southward transport is weakened when the oceanic SACZ is established. This is verified by comparing the volume transport of -18.37 Sv in Figure S1b, where we used the 3-day averages meridional current prior to the SACZ episodes. An intermediate value of volume transport -16.98 Sv is found for the three months of simulations used in this study (Figure S1c). Our transport results agree with those shown in Figure 1 of Schmid and Majumder (2018), which are based in several scientific articles.

This analysis revealed a strong indication that the horizontal advection of temperature is one of the candidates involved in the oceanic dynamics of surface ocean cooling, and this is analyzed in more detail in the heat budget analysis presented in Section 4.

It is important to remark that the colder surface waters are not only underneath the oceanic SACZ position, as given by the OLR plots. They are also present southwards and southwestwards of the oceanic SACZ position, showing that the dynamical effect of the atmospheric surface circulation associated with the oceanic SACZ, is not restricted to the region underneath its cloud band. Also, it should be noted that CVSS presence is one of the causes of the intensification of the oceanic portion of the SACZ as shown in Rosa et al. (2020), as well as the oceanic surface cooling southwest of it.

## 4. Ocean Mixed Layer Heat Balance

In addition to the dynamical effects discussed above, air-sea radiative (short and long wave radiation) and turbulent (latent and sensible) heat fluxes at the surface, or their net result ( $Q_{net}$ ) are key elements contributing thermodynamically to the temperature of surface layer waters. In an effort to understand and evaluate the SACZ impacts on the ocean surface waters, the ocean mixed layer heat balance for this area was calculated following similar approaches used in McPhaden et al. (1991), Wilkin (2006), Marchesiello et al. (2010), Foltz et al (2013) and Tamsitt et al. (2016). To our knowledge, this is the first ocean mixed layer heat budget done for this region, for a case of an oceanic SACZ. The vertically integrated mixed layer heat storage equation used is given as (Dijkstra, 2008; Moisin and Niiler, 1998):

$$\rho c_p h \frac{\partial T_m}{\partial t} = \rho c_p h \left( -u_m \frac{\partial T_m}{\partial x} - v_m \frac{\partial T_m}{\partial y} - w_m \frac{dT_m}{dz} + k_h \nabla^2 T + k_v \frac{d^2 T}{dz^2} \right) \quad (3) \text{ and,}$$

$$\frac{Q_{net}}{\rho c_p} = k_v \frac{d^2 T}{dz^2} \text{ at } h = 0 \quad (4)$$

where  $Q_{net}$  is the surface net heat flux (positive is heat flux into the ocean),  $T_m$ ,  $u_m$ ,  $v_m$  and  $w_m$  are, respectively, the vertically averaged temperature, zonal, meridional and vertical velocity components in the mixed layer.  $\rho c_p h \frac{\partial T_m}{\partial t}$  is the heat storage ( $\text{Wm}^{-2}$ ) or temperature tendency  $\frac{\partial T_m}{\partial t}$  ( $^{\circ}\text{C s}^{-1}$ ),  $\rho$  is the water density ( $\text{kg m}^{-3}$ ),  $c_p$  is the water specific heat at constant pressure ( $\text{J kg}^{-1} ^{\circ}\text{C}^{-1}$ ). The first two terms on the right-hand side of the heat storage equation are lumped into a single horizontal heat advection term. The horizontal diffusive mixing (horizontal heat diffusion) is the fourth term, and the vertical diffusive mixing (vertical heat diffusion) is the fifth term, and  $Q_{net}$  is applied as the surface boundary condition to this term. Specific heat of water at constant pressure ( $C_p$ ) and seawater density ( $\rho$ ) are assumed constant and as  $3.94 \times 10^3 \text{ Jkg}^{-1} ^{\circ}\text{C}^{-1}$  and  $10^3 \text{ kg m}^{-3}$ , respectively. The mixed layer depth  $h$  was calculated as the depth corresponding to a potential density ( $\sigma_{\theta}$ ) change of  $\Delta\sigma_{\theta} = 0.125 \text{ kg m}^{-3}$  relative to the most superficial level of the ocean model. This is the same methodology used by Monterey and Levitus (1997) and Cirano et al. (2006) in their global and Southwestern Atlantic Ocean analysis, respectively. A mean ocean mixed layer heat balance for these cases was estimated by time averaging the terms in Equation 3 over the number of days of active oceanic SACZ episodes.

The terms of Equation 3 and their components are presented in Figures 7 and 8, except for the horizontal diffusion term, which was found to be very small (three orders of magnitude smaller than the other terms) and consequently was left out of this analysis. Examining the heat balance results from the individual SACZ cases (figures not shown), it was noticed that cases 1 to 3 were very similar in their patterns, leading us to conclude that they describe canonical features of oceanic SACZ cases. Based on that, it was decided to average the period of cases 1 to 3 (as shown in Table 1) considering this as a robust representation of the oceanic SACZ cases (Figures 7 and 8).

The major oceanic heat loss and cooling effect (represented by negative values, upward flux) is due to the evaporative latent heat flux (Figure 7a), which is followed by long wave radiation (Figure 7c), and by a smaller contribution from the sensible heat flux (Figure 7b). In normal conditions (no oceanic ZCAS) these three  $Q_{net}$  components are in large part compensated by the incoming short wave solar radiation (Figure 7d). However, in the area strongly affected by the oceanic SACZ there is a strong attenuation of short-wave heat flux at surface of the order of  $100$  to  $130 \text{ Wm}^{-2}$  due to the high cloud cover, as clearly seen in Figure 7d.

The sum of the individual surface heat flux terms ( $Q_{net}$ ), is presented in Figure 7e. Under the oceanic SACZ's offshore position, the surface net heat flux is either positive but near zero, or it is negative (white/light green shades in Figure 7e). This seems to be a combination of a reduction of incident shortwave radiation caused by the cloud cover associated with oceanic SACZ and mostly an increase of outgoing latent and sensible heat fluxes caused by a joint effect of lower humidity (negative moisture flux divergence; see Fig. 5i) and stronger offshore winds. Additionally, the slightly negative values around  $26^{\circ}\text{S}$  and  $42^{\circ}\text{W}$  in Figure 7e match with the cyclonic atmospheric vortex position (see Figure 5d) and are also in the southern edge of the cloud cover (see Figure 5e), indicating that the heat balance over this

region is a result of a complex interplay among Equation 3 terms, not simply a consequence of the oceanic SACZ cloud cover blocking the shortwave to reach the ocean surface (thermodynamic mechanism).

Some regions of higher negative values of surface sensible and latent heat fluxes can be observed south and close to the cloud band of the SACZ. It is likely that they are caused by an enhanced air-sea temperature difference induced by sea surface cooling produced by Ekman pumping and mesoscale eddies, also by regions of lower surface humidity modulated by moisture flux divergences and the presence of stronger surface winds (see e.g., wind plot in Figures and 5i) factors which enhance both, the sensible and the latent heat fluxes. To some extent, this is like what is shown in Figure 10 of Tirabassi et al. (2015) where near the coast there is a marked loss of heat through the air-sea fluxes. In addition, in their study it also extends farther south of the SACZ position. Our results also show that the net surface heat fluxes tend to cool the ocean underneath the cloud band (see Figures 5b, 5e, 5h) but the heat storage loss (Figure 8a) southwest of SACZ is due to a combination of net surface heat fluxes from other terms in the heat balance, related to the dynamic mechanism that will be further analyzed.

The sea surface cooling in Figures 5e, 6d and 6e underneath the SACZ is unquestionably due to the reduction of shortwave incidence at sea surface (shown in Figure 7d), as a consequence of increased cloud cover. This cooling mechanism is the same as suggested by Chaves and Nobre (2004) and Nobre et al. (2012) as the negative thermodynamic mechanism, as illustrated in Figure 1. This can be seen in Figure 7, where the negative values of net surface heat fluxes ( $Q_{net}$ ) are evident. This is the case when thermodynamics feedback is playing a role on the sea surface cooling. Chaves and Nobre (2004) have argued that the thermodynamic negative feedback is the main cooling process of the sea surface due to the SACZ's cloud band presence. In their study they argue that this thermodynamic effect is one order of magnitude ( $\sim 0.4^\circ\text{C}/\text{month}$ ) larger than the oceanic dynamic effect ( $\sim 0.02^\circ\text{C}/\text{month}$ ), caused by Ekman pumping. However, Chaves and Nobre (2004) calculated the effect of the dynamic heating/cooling of the SST considering only the vertical heat advection term caused by Ekman Pumping, whereas here we consider advection (horizontal and vertical) and a changing mixed layer depth. In addition, their work was made over 120 consecutive days, which includes days of active SACZ and days without SACZ, while here, through case selection, only active SACZ days are used. This may explain the difference from our results, where the heat budget clearly shows that vertical mixing and horizontal advection in Figures 8b to 8c are as important as the air-sea heat fluxes in controlling the SST variability, as well as the negative feedbacks associated with it.

Those two terms (Figure 8b to 8c) have the same order of magnitude as the surface heat fluxes (Figure 7e). The stronger green shaded negative values shown in Figure 8b and 8c are approximately located where Ekman pumping is active (yellow/red values in Figure 6b), showing the importance of this dynamic process (i.e., vertical mixing) in controlling the surface water temperatures. We can see that both vertical mixing and horizontal advection are contributing to intensify the surface temperature decreases seen in Figure 8a via the oceanic mixed layer heat budget. This behavior occurs for all the three sets of simulations (not shown).

Negative heat advection effects seen in Figure 8c are present both in offshore open ocean regions and along the coast, except for some parts of São Paulo and Rio de Janeiro states. Considering its importance, it is worthwhile to discuss the possible ways in which the horizontal advection of temperature can be changed. In contrast to the other terms of heat budget equation, which are mostly local (they can be estimated at each grid point regardless of the neighboring grid points), the horizontal advection depends not only on the local vector current, but also on the temperature gradient field, which is determined by the neighboring grid points. Even in a situation in which the flow field is stationary, changes in the temperature field (caused inhomogeneous surface heat fluxes or dynamical ocean processes) will change the temperature gradient field and consequently the scalar product of the flow field with it and the horizontal advection. Another important way of modulating the horizontal advection is by the changes of horizontal flow field induced by the presence of mesoscale eddies. Regions where the mesoscale flow is up the temperature gradient are regions of negative horizontal advection and will contribute to cooling.

Therefore, the cooling seen underneath the SACZ position (and south of it) has a contribution from the horizontal advection (Figure 8c), which is produced by a combination of the mesoscale eddy field flow changes, and temperature modulation produced by eddy induced upwelling at their cores and vertical flow produced by Ekman pumping dynamics associated with the curl of surface wind.

A decrease of surface water velocity of the Brazil Current and its southward heat transport, as discussed in Section 3, will impact the heat balance, but the cause of this velocity decrease and its precise magnitude is still a matter for further studies. Near the shelf break and open oceanic regions negative advection terms of about  $-200 \text{ W.m}^{-2}$  are seen in a southwestward shifted region from the SACZ's position (Figure 8c), where  $Q_{net}$  values are positive (Figure 7e) and coincident with the absence of the cloud cover band region (Figure 3 and 4), around  $42^\circ\text{W}$  to  $39^\circ\text{W}$  and  $30^\circ\text{S}$  to  $26^\circ\text{S}$ . However, it must be noted that at this region, vertical mixing caused by CVSS is also playing a role on sea surface cooling, as seen in Figure 8b.

Our analysis of the ocean's thermal response based on the oceanic mixed layer heat balance shows that ocean-atmosphere interaction under the oceanic SACZ is very complex and cannot be simplified to being viewed as a merely a consequence of the reduced incident shortwave due to the cloud cover presence. Instead, ocean cooling processes are produced by both dynamics and thermodynamics. Our findings suggest that, contrary to what has been previously proposed, the thermodynamic processes through surface ocean-atmosphere fluxes, while important underneath the SACZ, are of the same magnitude as the ocean dynamic processes in controlling the SST of that region. In this region the horizontal advection plays a significant role. Moreover, to the south of it, both horizontal advection and Ekman pumping cause cooling, especially where the CVSS is located, as shown on the sequence of our results.

## 5. Final Remarks And Conclusions

Our results show that oceanic SACZ episodes strongly modulate the SST by a complex interplay of the combined effects from significant changes in both oceanic dynamics and thermodynamics in the mixed layer. The schematic diagram presented in Figure 9 summarizes the main physical ideas of ocean-atmosphere interactions present during ocean SACZ episodes, as well as the findings of our investigation that are discussed below.

The low-level atmospheric circulation and associated air-sea flux modification caused by the convergence of humidity flux, together with changes in the Ekman pumping and eddy dynamics, and the presence of an extensive cloud cover band over Southwest Atlantic Ocean result in sea surface water cooling through dynamic and thermodynamic mechanisms (Figure 1). As shown in the ocean mixed layer heat balance and Ekman pumping calculations, horizontal advection and vertical mixing (as part of dynamic mechanism) have the same order of magnitude as the net surface heat fluxes (as part of the thermodynamic mechanism). The surface atmospheric circulation patterns established during oceanic SACZ cases seems to promote a reduction of the heat transport to the south associated with the Brazil Current and neighboring offshore waters. An enhancement of the mesoscale eddy field seems to be produced with the net effect of reversing the direction of the horizontal heat transport in various regions affected by the oceanic SACZ. This can be seen from the heat budget's results (Section 5) combined with the joint analysis of the current and the SST in Figure 6c, and mainly from their tendencies in Figure 6e (Section 4).

On the region right underneath the oceanic SACZ, contrary to what was previously thought and reported in the literature, upwelling is not a major player on causing surface cooling, even though it is caused by well-established dynamic atmospheric circulation (Figure 6b) and has shown its presence in dynamic oceanic analysis (Figure 8b). We suggest that the surface cooling by Ekman upwelling underneath the cloud band does not occur because the water just below the mixed layer bottom in that region is not colder than the first layers of the ocean as our simulations indicate (figures not shown).

A striking feature found in this study is the presence of a cyclonic atmospheric vortex (previously defined as CVSS) both at the surface and aloft at 850 hPa, south of the SACZ. The surface atmospheric circulation established by CVSS produces a surface water cooling southwest of the SACZ position that seems to be produced by a divergent surface layer Ekman transport. This cyclonic atmospheric system is rarely discussed in the literature: right underneath it, the model results show a large area of cooled surface waters, as well as decreased air humidity, indicated by the positive humidity flux divergence. Rosa et al. (2020) found that during continental SACZ episodes there is a trough near the Uruguayan coast but during oceanic SACZ episodes this trough closes into a cyclonic vortex positioned southwest of the SACZ, accompanied by an intensification and northward displacement of the SACZ cloud band. According to our present results, the proposed mechanism of shortwave - SST negative thermodynamic feedback (Figure 1b and represented on schematic in Figure 9) apparently is not acting alone on oceanic surface cooling, as previously argued in the literature (e.g. Chaves and Nobre (2004); Chaves and Satyamurty, 2006; Almeida et al. 2007; Nobre et al., 2012, among others). The analysis of intense oceanic SACZ episodes here presented shows that oceanic dynamics, as seen in our ocean mixed layer heat

balance analysis through vertical mixing and horizontal advection, significantly contributes to oceanic surface cooling underneath of SACZ position. In addition, this dynamical mechanism is dominating the cooling to the southwest of the SACZ, (Figure 5h) where the CVSS (Figure 5g) is producing a cyclonic wind stress circulation (Figure 6b) that induces horizontal advection and upward water movement seen in  $w_E$  and in the vertical velocity simulated by the ocean model (Figure 6c). The oceanic analysis of this phenomenon was complemented by the calculation of the thermal balance terms in the ocean mixed layer, which elucidated the role of horizontal advection (Figures 6c to 6e and 7c) as an important player in the surface cooling of the ocean.

This cooling caused by horizontal advection in that region is a noteworthy new result of this study. It is our belief that the results obtained here do not totally reveal the full interplay of ocean-atmosphere interactions in oceanic SACZ episodes modulating the oceanic dynamics and thermodynamics. Nevertheless, our results expand upon previous knowledge about the SACZ, and bring out new points for further investigations, both in modeling and observations, and stressing the need for considering the SST changes because of modifications caused by oceanic dynamics.

We conclude this work by emphasizing the importance of this region for the Brazilian economy. Most of the Brazilian oil exploration and production is concentrated in this region (Marta-Almeida, 2013; IBAMA, 2019). Another important aspect is related to natural resources, such as fishing for example (Soares et al., 2011), which is extremely active in this region. A better understanding of the response of this oceanic area to changes in air-sea interaction processes and ocean circulation associated is needed for underpinning studies of larvae dispersion and for understanding connectivity between large marine ecosystems of the region (Soares et al., 2011, Dias et al., 2014, D'Agostine et al. 2015). Episodes of oceanic SACZ may also influence the pathways of pollutants such as oil spills and floating litter and micro-plastic particles.

## Declarations

## Competing interests

The authors declare no competing interests.

## Acknowledgements

This research was funded by the Brazilian agencies CAPES, CNPq, and FAPESP upon the following projects: Antarctic Modeling and Observation System (CNPq/PROANTAR 443013/2018-7), Advanced Studies in Oceanography of Medium and High Latitudes (CAPES 23038.004304/2014-28). FAPESP is acknowledged for funding L. P. Pezzi scientific visit to CASPO Division of the Oceans and Atmosphere Section of the Scripps Institution of Oceanography, University of California, San Diego, La Jolla, CA, USA, during June and July 2016 (FAPESP 2016/02710-3). CNPq funds L. P. Pezzi through fellowship of the Research Productivity Program (CNPq 304858/2019-6). AJM was partly supported by the National

Science Foundation (OCE-2022868). We thank Dr. John C. Warner and all the colleagues who work developing the COAWST modeling system and for providing their open access codes. The Uninterpolated OLR data provided by the NOAA/OAR/ESRL PSD, Boulder, Colorado, USA, from their web site at [http://www.esrl.noaa.gov/psd/data/gridded/data.uninterp\\_OLR.html](http://www.esrl.noaa.gov/psd/data/gridded/data.uninterp_OLR.html). The Global Satellite Mapping of Precipitation (GSMaP) from combined passive microwave and infrared radiometric data can be obtained information at <https://sharaku.eorc.jaxa.jp/GSMaP/guide.html>. Updated daily NCEP Climate Forecast System Version 2 (CFSv2) 6-hourly products were obtained in Research Data Archive at the National Center for Atmospheric Research, Computational and Information Systems Laboratory. <https://doi.org/10.5065/D61C1TXF>. Accessed 21 Sep. 2021. Simple Ocean Data Assimilation v 3.3.1 (SODA) can be accessed in <http://www.atmos.umd.edu/~ocean>. The National Centers for Environmental Prediction (NCEP) Final Operational Global Analysis (FNL) can be accessed in <http://rda.ucar.edu/datasets/ds083> provided the atmospheric lateral boundaries. The authors also thank two anonymous reviewers whose comments greatly helped to improve the manuscript.

## References

1. Almeida, R. A. F., P. Nobre, R. J. Haarsma, and E. J. D. Campos, 2007: Negative ocean atmosphere feedback in the South Atlantic Convergence Zone. *Geophys. Res. Lett.*, **34**, L18809.
2. Arruda, R., P. H. R. Calil, A. A. Bianchi, S. C. Doney, N. Gruber, I. Lima, and G. Turi, 2015: Air– sea CO<sub>2</sub> fluxes and the controls on ocean surface pCO<sub>2</sub> variability in coastal and open-ocean southwestern Atlantic Ocean: a modeling study, *Biogeosciences Discuss*, **12**, 7369–7409, doi:10.5194/bgd-12-7369-2015.
3. Assireu, A.T., M. R. Stevenson, and J. L. Stech, 2003: Surface circulation and kinetic energy in the SW Atlantic obtained by drifters. *Cont. Shelf Res.*, **23**, 145–157.
4. Barreiro, M., P. Chang, and R. Saravanan, 2002: Variability of the South Atlantic Convergence Zone Simulated by an Atmospheric General Circulation Model. *J. Climate*, **15**, p. 745-763.
5. Bender, M.A., I. Ginis, R. Tuleya, B. Thomas, and T. Marchok, 2007: The operational GFDL coupled hurricane–ocean prediction system and a summary of its performance. *Mon. Wea. Rev.*, **135**, 3965–3989.
6. Bender, M.A., and I. Ginis, 2000: Real-case simulations of hurricane–ocean interaction using a high-resolution coupled model: effects on hurricane intensity. *Mon. Wea. Rev.*, **128**, 917–946.
7. Booij, N., R. C. Ris, and L. H. Holthuijsen, 1999: A third-generation wave model for coastal regions, Part I: Model description and validation, *J. Geophys. Res.*, **104**, C4, 7649-7666.
8. Bombardi, R. J., L. M. V. Carvalho, C. Jones, M. S. Reboita, 2014a. Precipitation over eastern South America and the South Atlantic Sea surface temperature during neutral ENSO periods. *Climate Dynamics*, **42**:1553–1568. doi: 10.1007/s00382-013-1832-7.
9. Bombardi, R. J., L. M. V. Carvalho, C. Jones, 2014b: Simulating the influence of the South Atlantic dipole on the South Atlantic convergence zone during neutral ENSO. *Theoretical and applied climatology*, **118**(1), pp.251-269. doi: 10.1007/s00704-013-1056-0

10. Brasiliense, C. S., C. P. Dereczynski, P. Satyamurty, S. C. Chou, V. R. S. Santos, and R. N. Calado, 2017: Synoptic analysis of an intense rainfall event in Paraíba do Sul river basin in southeast Brazil. *Meteor. Appl.*, **25**, 66-77, doi:10.1002/met.1670.
11. Calil, P.H.R.; Suzuki, N.; Baschek, B.; da Silveira, I.C.A. Filaments, Fronts and Eddies in the Cabo Frio Coastal Upwelling System, Brazil. *Fluids* 2021, *6*, 54. <https://doi.org/10.3390/fluids6020054>. Carton, J.A., and B.S. Giese, 2008: A reanalysis of ocean climate using Simple Ocean Data Assimilation (SODA). *Mon. Wea. Rev.*, **136**, 2999-3017.
12. Carvalho, L. M. V., C. Jones, and B. Liebmann, 2002: Extreme precipitation events in southeastern South America and large-scale convective patterns in the South Atlantic convergence zone. *J. Climate*, *15*, 2377–2
13. Carvalho, L. M. V., C. Jones, and B. Liebmann, 2004: The South Atlantic Convergence Zone: Intensity, Form, Persistence, and Relationships with Intraseasonal and Interannual Activity and Extreme Rainfall. *J. Climate*, **17**, 88-108, [https://doi.org/10.1175/1520-0442\(2004\)017<0088:TSACZI>2.0.CO;2](https://doi.org/10.1175/1520-0442(2004)017<0088:TSACZI>2.0.CO;2).
14. Casarin, D. P., and V. E. Kousky, 1986: Precipitation anomalies in the southern part of Brazil and variations of the atmospheric circulation. *Revista Brasileira de Meteorologia*, **1**, 83-90.
15. Castelão, R. M and Barth, J. A. Upwelling around Cabo Frio, Brazil: The importance of wind stress curl. *Geophysical Research Letters*. VOL. 33, L03602, doi:10.1029/2005GL025182, 2006.
16. Castro, B.M, 2014: Summer/winter stratification variability in the central part of the South Brazil Bight. *Cont. Shelf Res.*, **89**, 15–23.
17. Castro, B.M., and L. B. Miranda, 1998: Physical oceanography of the western Atlantic continental shelf located between 4°N and 34°S, *The Sea*, K. H. Robinson, and K. H. Brink, Eds., Wiley, Berlin, Germany 209-251.
18. Cerda, C., and B. M. Castro, 2014: Hydrographic climatology of South Brazil Bight shelf waters between Sao Sebastião (24S) and Cabo São Tome(21S). *Cont. Shelf Res.*, **89**, 5–14.
19. Cergole, M.C., S. A. Saccardo and C. L. D. B. Rossi-Wongtschowski, 2002: Fluctuation in the spawning stock biomass and recruitment of the brazilian sardine (*Sardinella brasiliensis*) 1977-1997. *Rev. Bras. Oceanogr.*, **50**, 13-26.
20. Chaves, R. R., and P. Nobre, 2004: Interactions between sea surface temperature over the South Atlantic Ocean and the South Atlantic Convergence Zone. *Geophys. Res. Lett.*, **31**, L03204.
21. Chaves, R. R. and P. Satyamurty, 2006: Estudo das condições regionais associadas a um evento de forte ZCAS em janeiro de 2003. *Revista Brasileira de Meteorologia*, **21**, n.1, 134-140.
22. Chen, F., and J. Dudhia, 2001: Coupling an advanced land surface-hydrology model with the Penn State-NCAR MM5 modeling system. Part I: Model description and implementation. *Mon. Wea. Rev.*, **129**, 569-585.
23. Chen, S.S., J. F. Price, W. Zhao, M. A. Donelan, and E. J. Walsh, 2007: The CBLAST- Hurricane program and the next-generation fully coupled atmosphere-wave-ocean models for hurricane research and prediction. *Bull. Amer. Meteor. Soc.*, **88**, 311–317.

24. Chou, M. D., and M. J. Suarez, 1999: Solar radiation parameterization for atmospheric research studies. NASA Tech. Memo. NASA/TM-1999-104606, NASA/Laboratory for Atmospheres and Laboratory for Hydrospheric Processes, Washington, DC, 40 pp. [Available online at <https://gmao.gsfc.nasa.gov/pubs/docs/Chou136.pdf>].
25. Cirano, M., M. M. Mata, E. J. D. Campos, N. F. R. Deiró, 2006: A circulação oceânica de larga-escala na região oeste do Atlântico Sul com base no modelo de circulação global OCCAM. *Rev. Bras. Geof.*, **24(2)**, 209–230.
26. Combes, V., and R. P. Matano, 2014: A two-way nested simulation of the oceanic circulation in the Southwestern Atlantic, *J. Geophys. Res. Oceans*, **119**, 731–756, doi:10.1002/2013JC009498.
27. D'Agostini, A, D. F. M. Gherardi, L. P. Pezzi, 2015: Connectivity of Marine Protected Areas and Its Relation with Total Kinetic Energy. *PLoS ONE*, **10(10)**, e0139601, doi:10.1371/journal.pone.0139601.
28. Dias D. F, L. P. Pezzi, D. F. M. Gherardi, and R. Camargo, 2014: Modeling the Spawning Strategies and Larval Survival of the Brazilian Sardine (*Sardinella brasiliensis*). *Progress in Oceanography*, **123**, 38–53, doi: 10.1016/j.pocean.2014.03.009.
29. Dijkstra, H.A., 2008: Dynamical Oceanography. Springer-Verlag, 407pp.
30. Endo, C.A.K., Gherardi, D.F.M., Pezzi, L. P., Lima, L. N. Low connectivity compromises the conservation of reef fishes by marine protected areas in the tropical South Atlantic. *Sci Rep* **9**, 8634 (2019). <https://doi.org/10.1038/s41598-019-45042-0>
31. Figueroa, S. N., and C. A. Nobre, 1990: Precipitation distribution over central and western tropical South America. *Climanálise*, **5**, 36-45.
32. Ferreira, N. J., M. Sanches., M. A. F. Silva Dias, 2004: Composição da Zona de Convergência do Atlântico Sul em Períodos de El Niño e La Niña. *Revista Brasileira de Meteorologia*, **19**, n.1, 89-98.
33. Foltz, G. R., Schmid, C. and Lumpkin, R. 2013. Seasonal Cycle of the Mixed Layer Heat Budget in the Northeastern Tropical Atlantic Ocean. *Journal of Climate*. Doi: 10.1175/JCLI-D-13-00037.1
34. Gan, M. A., L. R. Rodrigues, and V. B. Rao, 2009: Monção na América do Sul. *Tempo e Clima no Brasil*. Cavalcanti, I. F. A., N. J. Ferreira, M. G. A. J. Silva, and M. A. F. Silva Dias, Eds., Oficina de Textos, 297-316.
35. Gigliotti, E. S., D. F. M. Gherardi, E. T. Paes, R. B. Souza and M. Katsuragawa, 2010: Spatial analysis of egg distribution and geographic changes in the spawning habitat of the Brazilian sardine *Sardinella brasiliensis*. *J. Fish. Biol.*, **77**, 2248-2267, doi:10.1111/j.1095-8649.2010.02802.x.
36. Goes, M., Cirano, M., Mata, M. M., & Majumder, S. (2019). Long-term monitoring of the Brazil Current transport at 22°S from XBT and altimetry data: Seasonal, interannual, and extreme variability. *Journal of Geophysical Research: Oceans*, 124. <https://doi.org/10.1029/2018JC014809>
37. Grimm, A. M., 2011: Interannual climate variability in South America: impacts on seasonal precipitation, extreme events and possible effects of climate change. *Stochastic Environmental Research and Risk Assessment*, **25**, n.4, 537-554, doi:10.1007/s00477-010-0420-1.
38. Grimm, A. M., J. Pal, and F. Giorgi, 2007: Connection between spring conditions and peak summer monsoon rainfall in South America: Role of soil moisture, surface temperature, and topography in

- eastern Brazil. *J. Climate*, **20**, 5929-5945.
39. Grimm, A. M., and P. L. Silva Dias, 1995: Analysis of tropical-extratropical interactions with influence functions of a barotropic model. *J. Atmos. Sci.*, **52**, 3538-3555.
40. Grimm, A. M., and M. T. Zilli, 2009: Interannual variability and seasonal evolution of summer monsoon rainfall in South America. *J. Climate*, **22**, 2257-2275.
41. Haidvogel, D. B., H. G. Arango, W. P. Budgell, B. D. Cornuelle, E. Curchi-T-Ser, E. Di Lorenzo, K. Fennel, W. R. Geyer, A. J. Hermann, L. Lanerolle, J. Levin, J. C. McWilliams, A. J. Miller, A. M. Moore, T. M. Powell, A. F. Shchepetkin, C. R. Sherwood, R. P. Signel, J. C. Warner and J. Wolkin, 2008: Regional ocean forecasting in terrain-following coordinates: model formulation and skill assessment. *J. Comp. Phys.*, **227**, 3595–3624.
42. Hirata, F. E. e A. M. Grimm, 2015: The role of synoptic and intraseasonal anomalies in the life cycle of summer rainfall extremes over South America. *Climate Dynamics*, DOI: 10.1007/s00382-015-2751-6
43. IBAMA. Technical note. Informação técnica no 7/2019-coprod/cgmac/dilic. Online (2019). [https://www.ibama.gov.br/phocadownload/notas/2019/informacaotecnica\\_n\\_7\\_2019.pdf](https://www.ibama.gov.br/phocadownload/notas/2019/informacaotecnica_n_7_2019.pdf). Accessed 12 March 2021
44. Jacob, R., J. Larson, and E. Ong, 2005: MN Communication and Parallel Interpolation in Community Climate System Model Version 3 using the model coupling toolkit. *Int. J. H. Perf. Comp. App.*, **19**, 293-307.
45. Janjić, Z. I., cited 2002: Nonsingular implementation of the Mellor-Yamada level 2.5 scheme in the NCEP meso model. [Available online at <http://www.emc.ncep.noaa.gov/officenotes/newernotes/on437.pdf>].
46. Jones, P. W., cited 1998: A Users Guide for SCRIP: A Spherical Coordinate Remapping and Interpolation Package. [Available online at <http://climate.lanl.gov/Software/SCRIP/>].
47. Jones, C., and Horel, J. D., 1990: A circulação da Alta da Bolívia e a atividade convectiva sobre a América do Sul. *Revista Brasileira de Meteorologia*, **5**, 379-387.
48. Jorgetti, T., P. L. Silva Dias, and E. D. de Freitas, 2014: The relationship between South Atlantic SST and SACZ intensity and positioning. *Clim. Dyn.*, **42**, 3077-3086.
49. Kain, J. S., 2004: The Kain-Fritsch convective parameterization: An update. *J. Appl. Meteor*, **43**, 170-181.
50. Kalnay, E., K. C. Mo, and J. Paegle (1986), Large-Amplitude, Short-Scale Stationary Rossby Waves in the Southern Hemisphere: Observations and Mechanistic Experiments to Determine their Origin, *J. Atmos. Sci.*, **43**(3), 252-275.
51. Kalnay, E., K. C. Mo, and J. Paegle, 2004: Large Amplitude, Short Scale Stationary Rossby Waves in the Southern Hemisphere: Observations and Mechanistic Experiments to Determine their Origin. *J. Atmos. Sci.*, **43**, n.3, 252-275.
52. Kodama, Y., 1992: Large-scale common features of Sub-tropical Precipitation Zones (the Baiu Frontal Zone, the SPCZ, and the SACZ). Part I: characteristics of Subtropical Frontal Zones. *J. Meteor. Soc. Japan*, **70**, n.4, 813-835.

53. Kodama, Y., 1993: Large-scale common features of Sub-tropical Convergence Zones (The Baiu Frontal Zone, The SPCZ, and the SACZ). Part II: conditions of the circulation for generating the STCZs. *J. Meteor. Soc. Japan*, **71**, n.5, 581-610.
54. Kodama, Y. M., T. Suzuki, and Y. Takeuchi, 1997: Cloud clusters over the South Pacific, the South America and South Atlantic. Proceeding of Spring Assembly at Tsukuba. *J. Meteor. Soc. Japan*, p. 329.
55. Lang, S., W.-K. Tao, R. Cifelli, W. Olson, J. Halverson, S. Rutledge, and J. Simpson, 2007: Improving simulations of convective system from TRMM LBA: Easterly and westerly regimes. *J. Atmos. Sci.*, **64**, 1141-1164.
56. Larson, J., R. Jacob and E. Ong, 2005: The model coupling toolkit: A new Fortran90 toolkit for building multiphysics parallel coupled models. *International Journal of High Performance Computing Applications*, **19**, 277-292.
57. Legeckis, R., and A. L. Gordon, 1982: Satellite observations of the Brazil and Falkland Currents 1975 to 1976 and 1978. *Deep-Sea Research*, **29**, 375-401.
58. Lesser, G. R., J. A. Roelvink, J. A. T. M. van Kester, and G. S. Stelling, 2004: Development and validation of a three-dimensional morphological model. *Coastal Engineering*, **51(8-9)**, 883-915.
59. Liebmann, G. N. Kiladis, J. A. Marengo, T. Ambrizzi, and J. D. Glick, 1999: Submonthly convective variability over South America and the South Atlantic convergence zone. *J. Climate*, **12**, 1977-1891.
60. Lima, I. D., C. A. E. Garcia, and O. O. Möller, 1996: Ocean surface processes on the southern Brazilian shelf: characterization and seasonal variability. *Cont. Shelf Res.*, **16**, 1307-1317.
61. Marengo, J. A., 2005: The characteristics and variability of the atmospheric water balance in the Amazon basin: Spatial and temporal variability. *Climate Dyn.*, **24**, 11-22.
62. Marchesiello, P., Lefèvre, J. Vega, A., Couvelard, X. and Menkes, C. (2010). Coastal upwelling, circulation and heat balance around New Caledonia's barrier reef. *Marine pollution bulletin*. 61. 432-448. [10.1016/j.marpolbul.2010.06.043](https://doi.org/10.1016/j.marpolbul.2010.06.043).
63. Marta-Almeida, M., Manuel Ruiz-Villarreal, M., Pereira, J. Pablo Otero, J., Cirano, M., Zhang, X., Hetland, R. (2013) Efficient tools for marine operational forecast and oil spill tracking. *Marine Pollution Bulletin*, Volume 71, Issues 1-2, 139-151, ISSN 0025-326X, <https://doi.org/10.1016/j.marpolbul.2013.03.022>.
64. Marton, E., 2000: Oscilações intrasazonais associadas a Zona de Convergência do Atlântico Sul no Sudeste Brasileiro. Ph. D. thesis, University of São Paulo. São Paulo [Available from Universidade de São Paulo, Av. Prof. Luciano Gualberto, 908, São Paulo, Brazil].
65. Matsuura, Y., 1998: Brazilian sardine (*Sardinella brasiliensis*) spawning in the southeast Brazilian Bight over the period 1976-1993. *Rev. Bras. Oceanogr.*, **46**, 33-43.
66. McTaggart-Cowan, R., L. F. Bosart, C. A. Davis, E. H. Atallah, J. R. Gyakum, and K. A. Emanuel, 2006: Analyses of Hurricane Catarina. *Mon. Weather Rev.*, **134**, 3029-3053, doi: 10.1175/MWR3330.1.
67. McPhaden, M. J. and Hayes, S. P., 1991: On the variability of winds, sea surface temperature, and surface layer heat content in the western equatorial Pacific. *J. Geophys. Res.*, **96**, 3331-3342,

doi:10.1029/90JC01726.

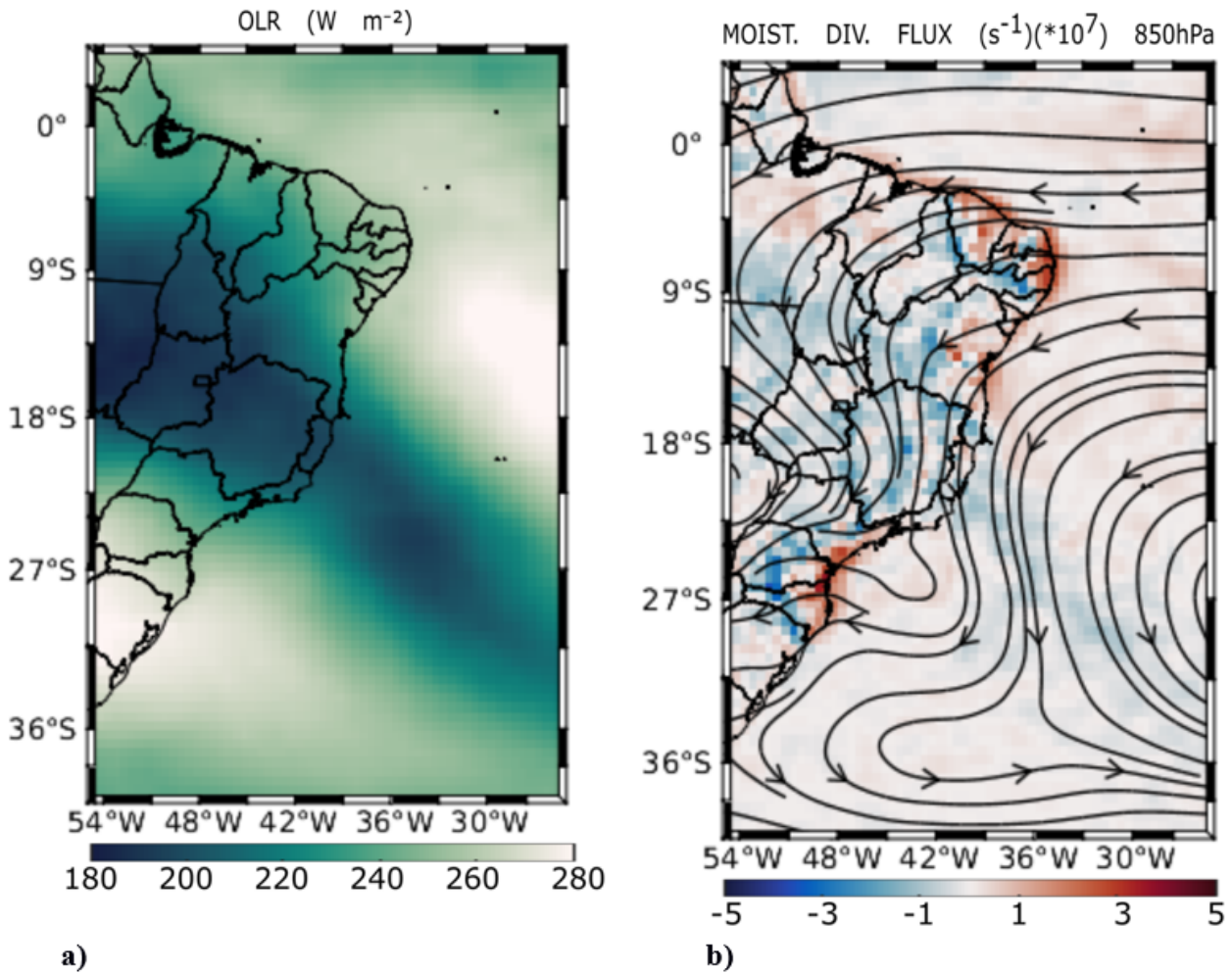
68. Mellor, G. L., and T. Yamada, 1982: Development of a turbulence closure model for geophysical fluid problems. *Rev. Geophys.*, **20**, 851-875.
69. Mendonça, L. F. M., R. B. Souza, C. R. C. Aseff, L.P. Pezzi, O. O. Möller, and R. C. M. Alvez, 2017: Regional modeling of the water masses and circulation annual variability at the Southern Brazilian Continental Shelf. *J. Geophys. Res. Oceans*, **122**, n2, 1232-1253, doi:10.1002/2016JC011780.
70. Miller, A. J., M. Collins, S. Gualdi, T. G. Jensen, V. Misra, L. P. Pezzi, D. W. Pierce, D. Putrasahan, H. Seo, and Y. Tseng, 2017: Coupled ocean-atmosphere modeling and predictions. THE SEA: THE SCIENCE OF OCEAN PREDICTION. *J. Mar. Res.*, **75**, 361-402.
71. Moisin, J.R. and P.P. Niiler, 1998: The seasonal heat budget of the North Pacific: Net heat flux and heat storage rates (1950-1990). *J. Phys. Oceanogr.*, **28**, 401-421.
72. Monin, A. S., and A. M. Obukhov, 1954: Basic laws of turbulent mixing in the surface layer of the atmosphere. *Contributions of the Geophysical Institute of the Slovak Academy of Sciences*, **24**, 163-187.
73. Monterey, G. I., and S. Levitus, 1997: Seasonal Variability of Mixed Layer Depth for the World Ocean. *NOAA Atlas NESDIS*, U.S. Gov. Printing Office, Wash., D.C., 96 pp.
74. National Centers for Environmental Prediction/National Weather Service/NOAA/U.S. Department of Commerce, 2000: NCEP FNL Operational Model Global Tropospheric Analyses, continuing from July 1999. Research Data Archive at the National Center for Atmospheric Research, Computational and Information Systems Laboratory, Boulder, CO. [Available online at <https://doi.org/10.5065/D6M043C6>.] Accessed 29 Jan 2018.
75. Nicholls, S. D., and Decker, S. G, 2015: Impact of coupling an Ocean Model to WRF Nor'easter Simulations. *Mon. Wea. Rev.*, **143**, 4997-5016.
76. Nobre, C. A., 1988: Ainda sobre a Zona de Convergência do Atlântico Sul: A importância do Oceano Atlântico. *Climanálise*, v. 3, n. 4, p. 30-33, 1988.
77. Nobre, P., R. Almeida, M. Malagutti, and E. Giarolla, 2012: Coupled Ocean-Atmosphere Variations over the South Atlantic Ocean. *J. Climate*, **25**, 6349-6358, doi:10.1175/JCLI-D-11-00444.1.
78. Nogués-Peagle, J., and E. K. C. Mo, 1997: Alternating wet and dry conditions over the South America during summer. *Mon. Wea. Rev.*, **125**, 279-291.
79. Palma, E. D., R. P. Matano, and A. R. Piola, 2008: A numerical study of the Southwestern Atlantic Shelf circulation: Stratified ocean response to local and offshore forcing, *J. Geophys. Res.*, **113**, C11010, doi:10.1029/2007JC004720.
80. Pezzi, L.P., R. B. Souza, O. Acevedo, I. Wainer, M. M. Mata, C. A. E. Garcia, and R. Camargo, 2009a: Multiyear measurements of the Oceanic and Atmospheric Boundary Layers at the Brazil-Malvinas Confluence Region. *J. Geophys. Res.*, **114**, D19103, doi:10.1029/2008JD011379.
81. Pezzi, L. P., R. B. Souza, M. S. Dourado, C. A. E. Garcia, M. M. Mata, and M. A. F. Silva-Dias, 2005: Ocean-atmosphere in situ observations at the Brazil-Malvinas Confluence region. *Geophys. Res. Lett.*, **32**, n.22, L22603, doi:10.1029/2005GL023866.

82. Pezzi, L. P., and R. B. Souza, 2009b: Variabilidade de meso-escala e interação Oceano-Atmosfera no Atlântico Sudoeste. *Tempo e Clima no Brasil*, I. F. A., N. J. Ferreira, M. G. A. J. Silva, and M. A. F. Silva Dias, Eds., Oficina de Textos, 385-405.
83. Pezzi, L. P., R. B. Souza, M. F. L. Quadro, 2016: A review on the ocean atmosphere interaction processes in regions of strong sea surface temperature gradients of the South Atlantic Ocean based on observational data. *Revista Brasileira de Meteorologia*, **31**, n.4, 428-453.
84. Pezzi, L. P., Souza, R.B., Santini, M.F. *et al.* Oceanic eddy-induced modifications to air–sea heat and CO<sub>2</sub> fluxes in the Brazil-Malvinas Confluence. *Sci Rep***11**, 10648 (2021).  
<https://doi.org/10.1038/s41598-021-89985-9>.
85. Pita, I. C., Cirano, M. and Mata, M. M. An assessment of Brazil Current surface velocity and associated transport near 22°S: XBT and altimetry data. *Regional Studies in Marine Science* 35 (2020) 101197.
86. Pullen, J., R. Allard, H. Seo, A. J. Miller, S. Chen, L. P. Pezzi, T. Smith, P. Chu, J. Alves, and R. Caldera, 2017: Coupled ocean-atmosphere forecasting at short and medium time scales. *The Science of Ocean Prediction*, Pinardi, N., P. Lermusiaux and K. Brink, **17**, p. 1,  
[doi:10.1357/002224017821836833](https://doi.org/10.1357/002224017821836833)
87. Putrasahan, D. A., A. J. Miller, and H. Seo, 2013a: Isolating mesoscale coupled ocean-atmosphere interactions in the Kuroshio Extension region. *Dynam. Atmos. Oceans*, **63**, 60–78.
88. Putrasahan, D. A., A. J. Miller, and H. Seo, 2013b: Regional coupled ocean-atmosphere downscaling in the Southeast Pacific: impacts on upwelling, mesoscale air-sea fluxes, and ocean eddies. *Ocean Dynam.*, **63**, 463–488.
89. Quadro, M. F. L., M. A. F. Silva Dias, D. L. Herdies, and L. G. G. Gonçalves, 2012: Análise Climatológica da Precipitação e do Transporte de Umidade na Região da ZCAS Através da Nova Geração de Reanálises. *Revista Brasileira de Meteorologia*, **27**, 152-162.
90. Quadro, M. F. L., L. P. Pezzi, and E. B. Rosa, 2016: O Climanálise e o monitoramento da ZCAS nos últimos 30 anos. *Rev. Climanálise*, **04**, 19-25.
91. Robertson, A. W., and C. R. Mechoso, 2000: Interannual and interdecadal variability of the South Atlantic Convergence Zone. *Mon. Wea. Rev.*, **128**, 2947-2957.
92. Rodrigues, R. R., and J. A. Lorenzetti, 2001: A numerical study of the effects of bottom topography and coastline geometry on the Southeast Brazilian coastal upwelling. *Cont. Shelf Res.*, **21(4)**, 371-394.
93. Rodrigues, R. R., and T. Woollings, 2017: Impact of Atmospheric Blocking on South America in Austral Summer. *J. Climate*, **30**, n.5, 1821-1837, [doi:10.1175/JCLI-D-16-0493.1](https://doi.org/10.1175/JCLI-D-16-0493.1).
94. Rodrigues, R.R., Taschetto, A.S., Gupta, A.S., and Foltz, G.R., 2019: Common cause for severe droughts in South America and marine heatwaves in the South Atlantic. *Nature Geoscience*, 12, 620-626,  
[doi.org/10.1038/s41561-019-0393-8](https://doi.org/10.1038/s41561-019-0393-8).

95. Rosa, E. B., 2017: Desempenho de um método automático para detecção de episódios de ZCAS. M. S. Thesis, Dept. of Remote Sensing, National Institute for Spatial Research, 131 pp., [Available online at <http://urlib.net/8JMKD3MGP3W34P/3NAANGP>]
96. Rosa E. B., Pezzi L. P., Quadro M. F. L. and Brunzell, N. (2020) Automated Detection Algorithm for SACZ, Oceanic SACZ, and Their Climatological Features. *Front. Environ. Sci.* 8:18. doi: 10.3389/fenvs.2020.00018
97. Satyamurty, P., C. Nobre, and P. L. Silva Dias, 1998: South America. *Meteorology of the Southern Hemisphere*, D. J. Karoly and D. G. Vincent, Eds., Amer. Meteor. Soc., 119–139.
98. Seo, H., 2017: Distinct influence of air-sea interactions mediated by mesoscale sea surface temperature and surface current in the Arabian Sea. *J. Climate*, **30**, 8061-8080, doi:10.1175/JCLI-D-16-0834.1
99. Seo, H., K. H. Brink, C. E. Dorman, D. Koracin, and C. A. Edwards, 2012: What determines the spatial pattern in summer upwelling trends on the U.S. West Coast?, *J. Geophys. Res.*, **117**, C08012, doi:10.1029/2012JC008016.
100. Seo, H., A. Miller and J. Roads, 2007: The Scripps Coupled Ocean-Atmosphere Regional (SCOAR) model, with applications in the eastern Pacific sector. *J. Climate*, **20**, 381–402.
101. Shchepetkin, A. F., and J. C. McWilliams, 2003: A method for computing horizontal pressure-gradient force in an oceanic model with a nonaligned vertical coordinate. *J. Geophys. Res.*, **108**, C3, 3090, doi:10.1029/2001JC001047.
102. Shchepetkin A. F., and J. C. McWilliams, 2005: The Regional Ocean Modeling System: a split-explicit, free-surface, topography-following coordinates ocean model. *Ocean Modelling*, **9**, 347–404.
103. Shi, J. J. and coauthors, 2010: WRF simulations of the 20-22 January 2007 snow events of eastern Canada: Comparison with in situ and satellite observations. *J. Appl. Meteor. Climatol.*, **49**, 2246-2266.
104. Silva, A. E., 2009: Variabilidade da Circulação e transporte umidade no Regime de Monção da America do Sul. Ph. D. thesis, University of São Paulo, São Paulo, 137 pp.
105. Skamarock W. C., J. B. Klemp, J. Dudhia, D. O. Gill, D. M. Barker, W. Wang, and J. G. Powers, 2005: A Description of the Advanced Research WRF Version 2. NCAR Tech. Note. NCAR/TN-468+STR, 88 pp.
106. Small, R. J., E. Curchitser, K. Hedstrom, B. Kauffman, and W. G. Large, 2015: The Benguela upwelling system: Quantifying the sensitivity to resolution and coastal wind representation in a global climate model, *J. Climate*, **28**, 9409–9432, doi:10.1175/JCLI-D-15-0192.1.
107. Soares, H. C., L. P. Pezzi, D. F. M. Gherardi, and E. T. Paes, 2011: Oceanic and atmospheric patterns during spawning periods prior to extreme catches of the Brazilian sardine (*Sardinella brasiliensis*) in the southwest Atlantic. *Scientia Marina*, **75**, 665–677.
108. Souza, R.B., and I. S. Robinson, 2004: Lagrangian and satellite observations of the Brazilian Coastal Current. *Cont. Shelf Res.*, **24**, 241–262.
109. Sunyé, P. S. and J. Servain, 1998: Effects of seasonal variations in meteorology and oceanography on the Brazilian sardine fishery. *Fish. Oceanogr.*, **7**, 89-100.

110. Sutil, U. A.; Pezzi, L. P. COAWST User's Guide - 3<sup>a</sup> Edition. São José dos Campos: INPE, 2020. 94 p., IBI: 8JMKD3MGP3W34R/43BQG8E, ISBN: 978-65-89159-00-1, doi:10.13140/RG.2.2.31269.12002. Available at: <http://urlib.net/8JMKD3MGP3W34R/43BQG8E>.
111. Talley L. D., G. L. Pickard, W. J. Emery, and J. H. Swift, 2011: *Descriptive Physical Oceanography: An Introduction*. 6d ed., Elsevier, 560 pp.
112. Tamsitt, V., L. D. Talley, M. R. Mazloff and I. Cerovecki, 2016: Zonal variations in the Southern Ocean heat budget. *J. Climate*, **29**, 6563-6579, doi:10.1175/JCLI-D-15-0630.1.
113. Tao, W.-K., J. J. Shi, S. S. Chen, S. Lang, P.-L. Lin, S.-Y. Hong, C. Peters-Ludard, and A. Hou, 2011: The impact of microphysical schemes on hurricane intensity and track. *Asia-Pac. J. Atmos. Sci.*, **47**, 1-16.
114. Taschetto, A. S. and I. Wainer, 2008 : The impact of the subtropical South Atlantic SST on South American precipitation. In *Annales Geophysicae*, **26** (11), 3457-3476.
115. Tirabassi, G., C. Masoller, and M. Barreiro, 2015: A study of the air-sea interaction in the South Atlantic Convergence Zone through Granger causality. *Int. J. Climatol.*, **35**, 3440-3453.
116. Ushio, T., K. SasaShige, T. Kubota, S. Shige, K. Okamoto, K. Aonashi, T. Inoue, N. Takahashi, T. Iguchi, M. Kachi, R. Oki, T. Morimoto, and Z.-I. Kawasaki, 2009: A Kalman filter approach to the Global Satellite Mapping of Precipitation (GSMaP) from combined passive microwave and infrared radiometric data. *J. Meteor. Soc. Japan*, **87A**, 137-151, doi:10.2151/jmsj.87A.137.
117. Wajsowicz, R.C., 1993: A consistent formulation of the anisotropic stress tensor for use in models of the large-scale ocean circulation. *J. Comput. Phys.*, **105**, 333-338.
118. Wallace, J. M., T. P. Mitchell, and C. J. Deser (1989), The influence of sea surface temperature on surface wind in the eastern equatorial Pacific: Weekly to monthly variability, *J. Clim.*, **2**, 1492– 1499.
119. Warner, J. C., B. Armstrong, R. He, and J. B. Zambon, 2010: Development of a Coupled Ocean-Atmosphere-Wave-Sediment Transport (COAWST) Modeling System. *Ocean Modelling*, **35**, 230-244.
120. Warner J. C., C. R. Sherwood, R. P. Signell, C. Harris, and H. G. Arango, 2008: Development of a three-dimensional, regional, coupled wave, current, and sediment-transport model. *Computers and Geosciences*, **34**, 1284-1306.
121. Warner, J. C., C. R. Sherwood, H. G. Arango, R. P. Signell: Performance of four turbulence closure models implemented using a generic length scale. *Ocean Model*, **8**, 81-113.
122. Wilkin, J., 2008: The summer time heat budget and circulation of southeast New England shelf waters, *J. Phys. Oceanogr.*, **36(11)**, 1997-2011.

## Figures



**Thermodynamic**



**Dynamic**

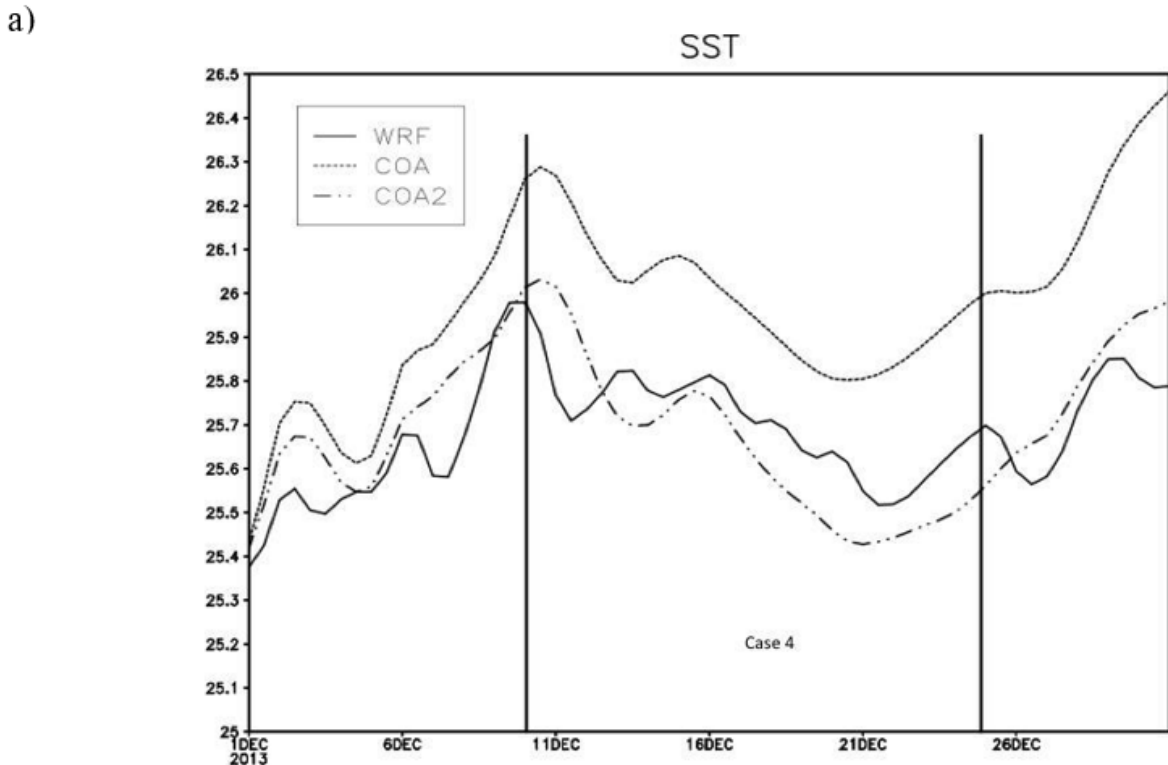
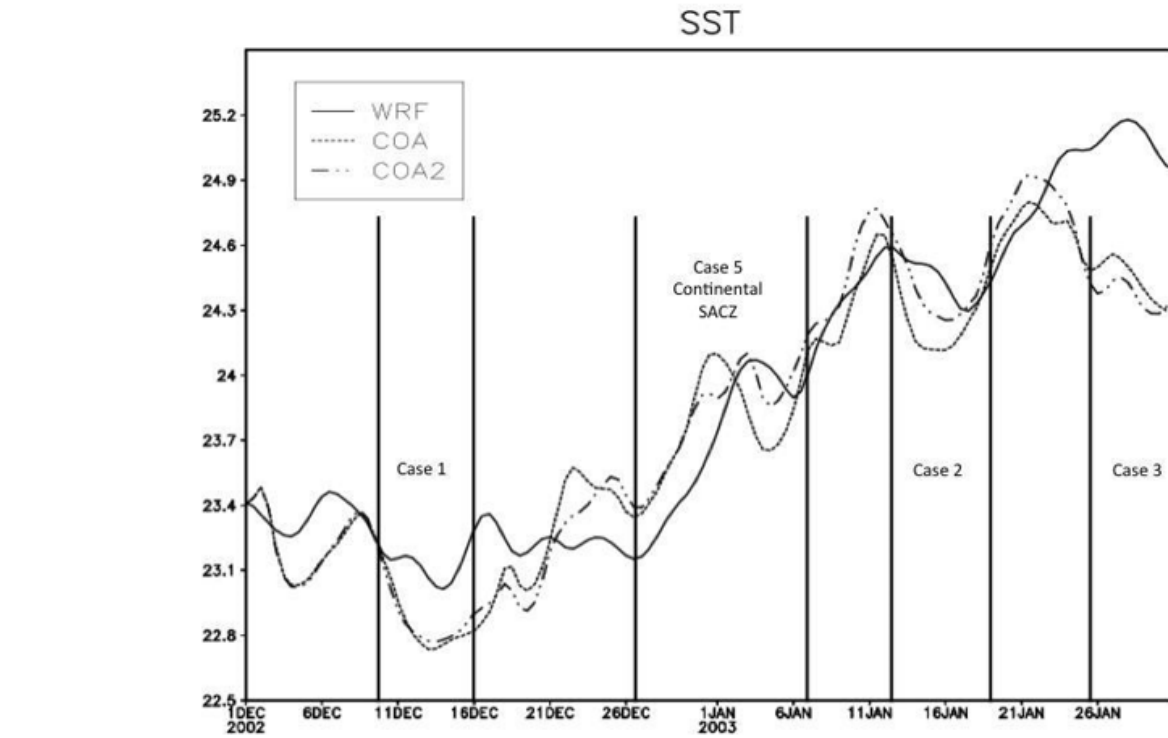


c)

**Figure 1**

a) Synoptic view for all four cases of oceanic SACZ using outgoing longwave radiation (OLR), units in  $W m^{-2}$ . b) Moisture flux divergence (colors in  $\times 10^7 s^{-1}$ ) and streamlines in 850 hPa. Both panels are made with CFSv2 reanalysis data set. c) Schematic representation of the physical processes involved in the modulation of SST in the oceanic layer when the oceanic SACZ is active. The thermodynamic process is

at the top and the dynamic process at the bottom of the figure. The up arrows indicate increase, and the down arrows decrease for each individual physical process.



b)

**Figure 2**

Time series showing SST area-averaged from 33°S to 20°S and 45°W to 35°W. Figure 1a includes the simulation from December 1<sup>st</sup> 2002 to January 31<sup>st</sup> 2003 while Figure 1b the simulation from December

1<sup>st</sup> 2013 to December 31<sup>st</sup> 2013. See Table 1 for the experiment's names and more details. Note that the WRF SST is prescribed and not simulated.

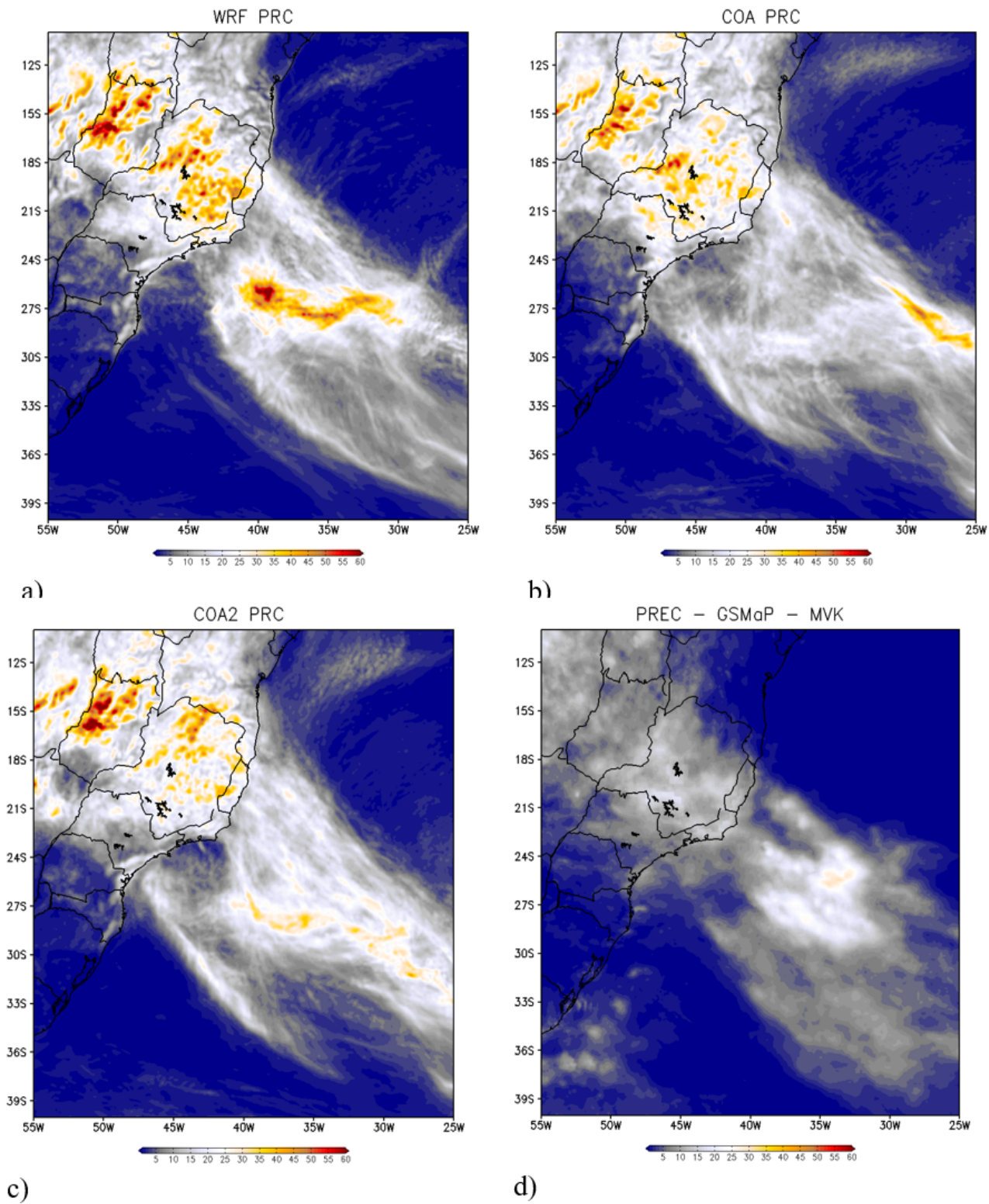
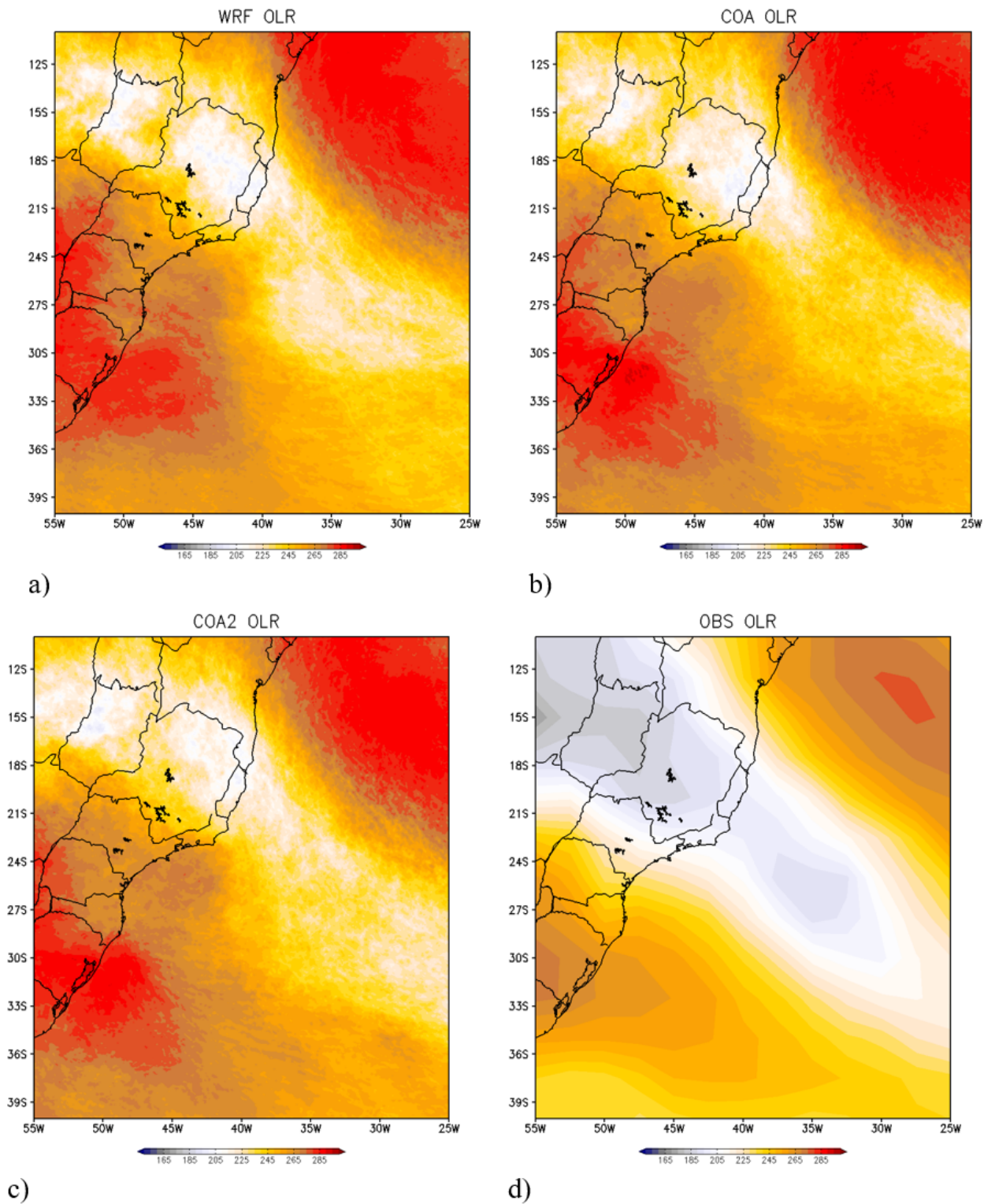


Figure 3

Mean precipitation for all four cases of the oceanic SACZ ( $\text{mm}\cdot\text{day}^{-1}$ ). Precipitation for (a) WRF, (b) COA, (c) COA2 and (d) Global Satellite Mapping of Precipitation (GSMaP), version MVK (GSMaP\_MVK).



**Figure 4**

Outgoing longwave radiation (OLR) for all four cases of oceanic SACZ (in  $\text{W m}^{-2}$ ). (a) OLR for WRF, (b) COA, (c) COA2 and (d) National Oceanic and Atmospheric Administration (NOAA) daily OLR.

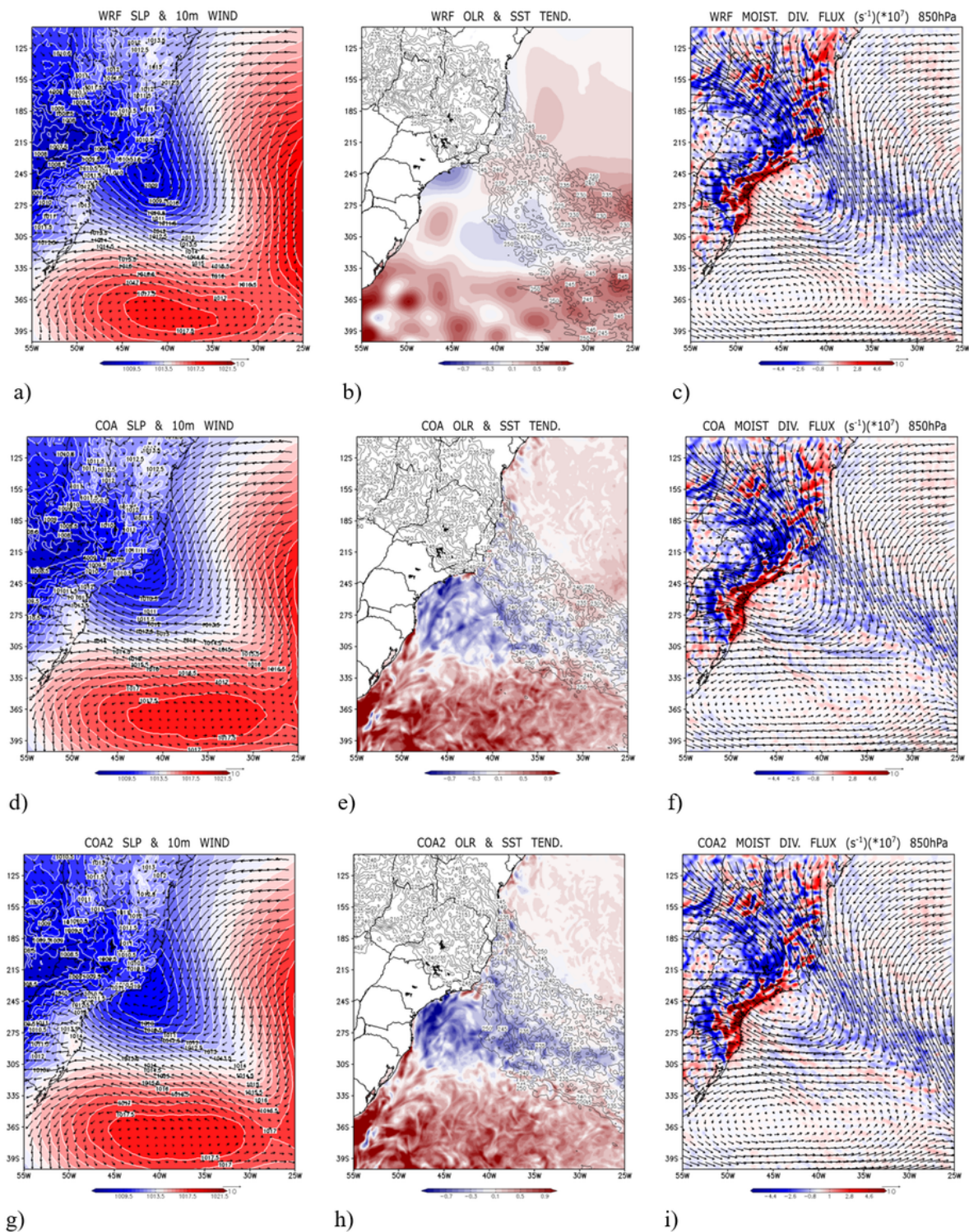


**Figure 5**

First column, (a), (d) and (g) shows WRF, COA, COA2, winds at 10 m height superimposed on SLP, in  $m \cdot s^{-1}$  and hPa, respectively. Second column, (b), (e) and (h) shows WRF, COA, COA2, respectively, SST tendency with OLR superimposed, in  $^{\circ}C \cdot day^{-1}$  and  $W \cdot m^{-2}$ . Third column, (c), (f), (i) shows for WRF, COA, COA2, respectively the moisture flux divergence with winds superimposed at 850 hPa, in  $1 \times 10^7 s^{-1}$  and  $m \cdot s^{-1}$ .

Colors indicate SLP in (a), (c), (e), SST tendency in (b), (d), (f) and moisture flux divergence in (c), (f) and (i). Note that WRF SST in panel (b) is prescribed and not simulated.

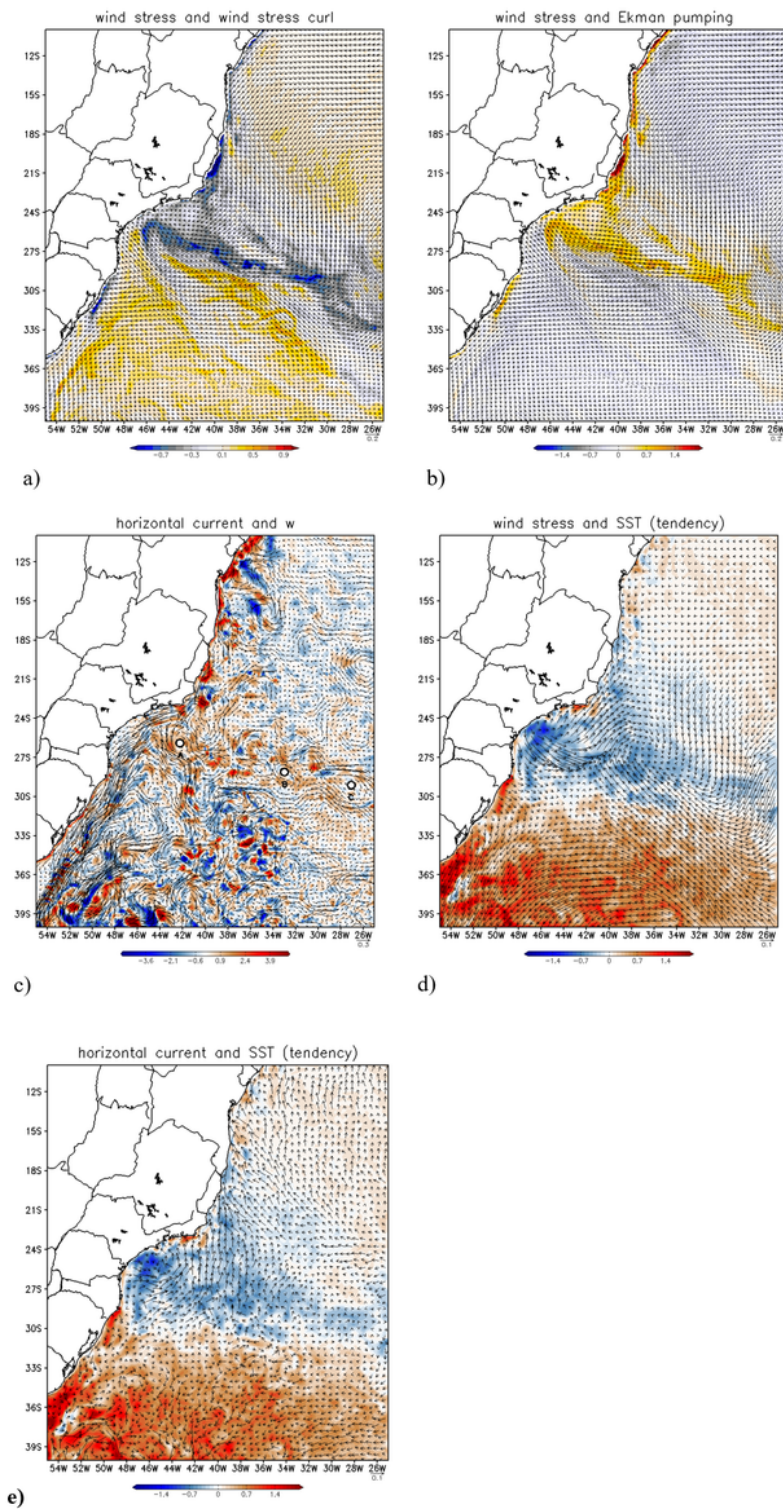


**Figure 6**

(a) Wind stress superimposed on wind stress curl (in  $\text{N.m}^{-2}$  and  $\times 10^{-6} \text{N.m}^{-2}$ ). (b) Wind stress superimposed on Ekman pumping as given by Equation 2 (in  $\text{N.m}^{-2}$  and  $\text{m.day}^{-1}$ ). (c) Oceanic horizontal

surface currents ( $\text{m}\cdot\text{s}^{-1}$ ) superimposed on oceanic vertical velocity ( $\text{m}\cdot\text{day}^{-1}$ ) where positive (negative) value indicates upward (downward) flow. The letter a, b and c denote three cyclonic eddies on the SACZ region discussed in the text. Difference between composites of oceanic SACZ episodes and 3 days average before for each episode, (d) SST ( $^{\circ}\text{C}$ ) and surface wind stress ( $\text{N}\cdot\text{m}^{-2}$ ) tendencies and (e) SST ( $^{\circ}\text{C}$ ) and surface oceanic currents ( $\text{m}\cdot\text{s}^{-1}$ ) tendencies. All results in this figure are from COA2, averaged for all four cases of oceanic SACZ.

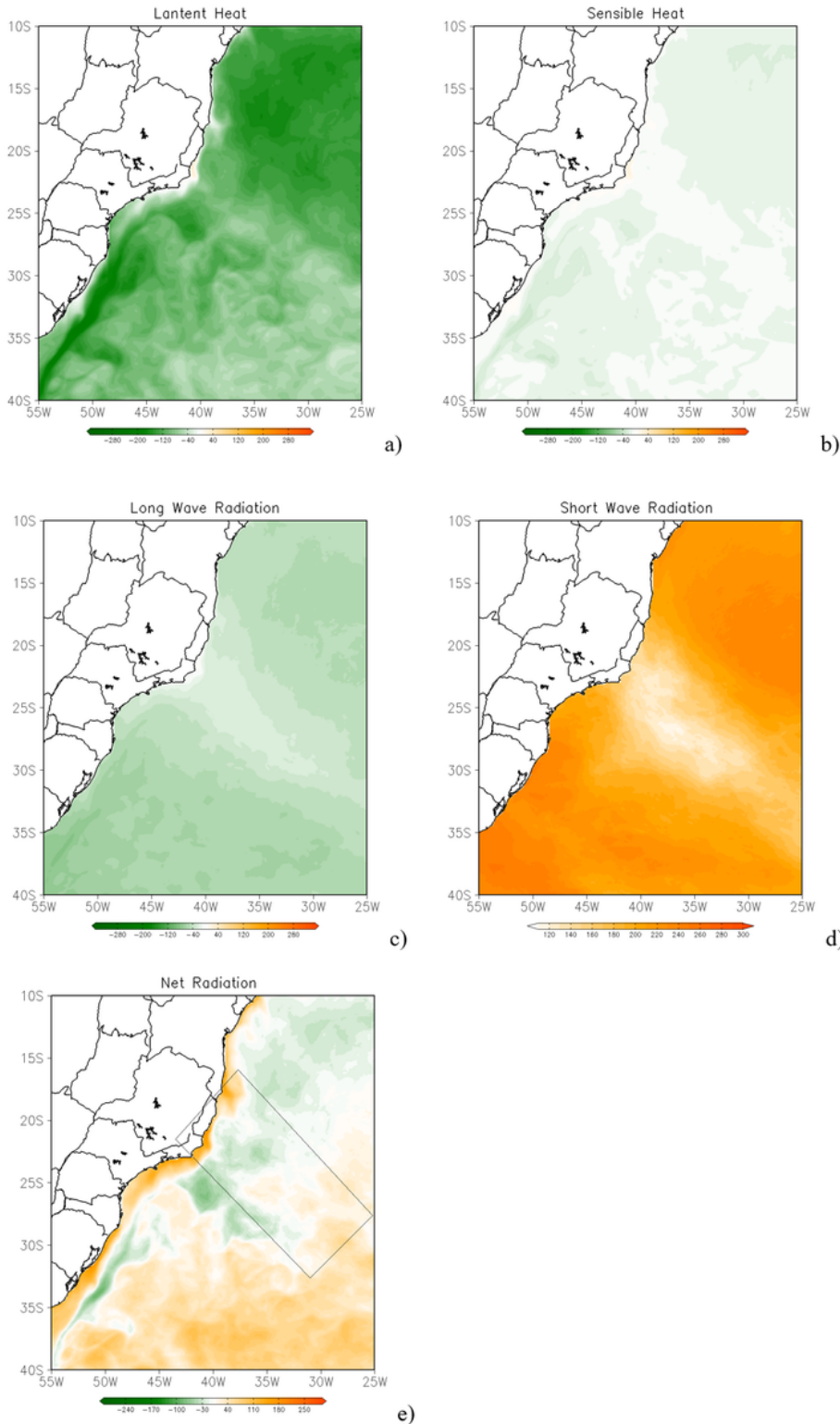


## Figure 7

Turbulent (latent and sensible) and radiational (short and long wave) vertical heat fluxes at surface and net heat flux ( $Q_{net}$ ), averaged in time for 1 to 3 SACZ cases, as indicated in the Table 1. (a) Latent heat flux. (b) Sensible heat flux. (c) Long wave radiation flux. (d) Short wave radiation flux (with color bar representing only positive values) . (e) Surface net heat flux ( $Q_{net}$ ). The panels in this figure were obtained from COA2 experiment. All fluxes are given in  $Wm^{-2}$ .

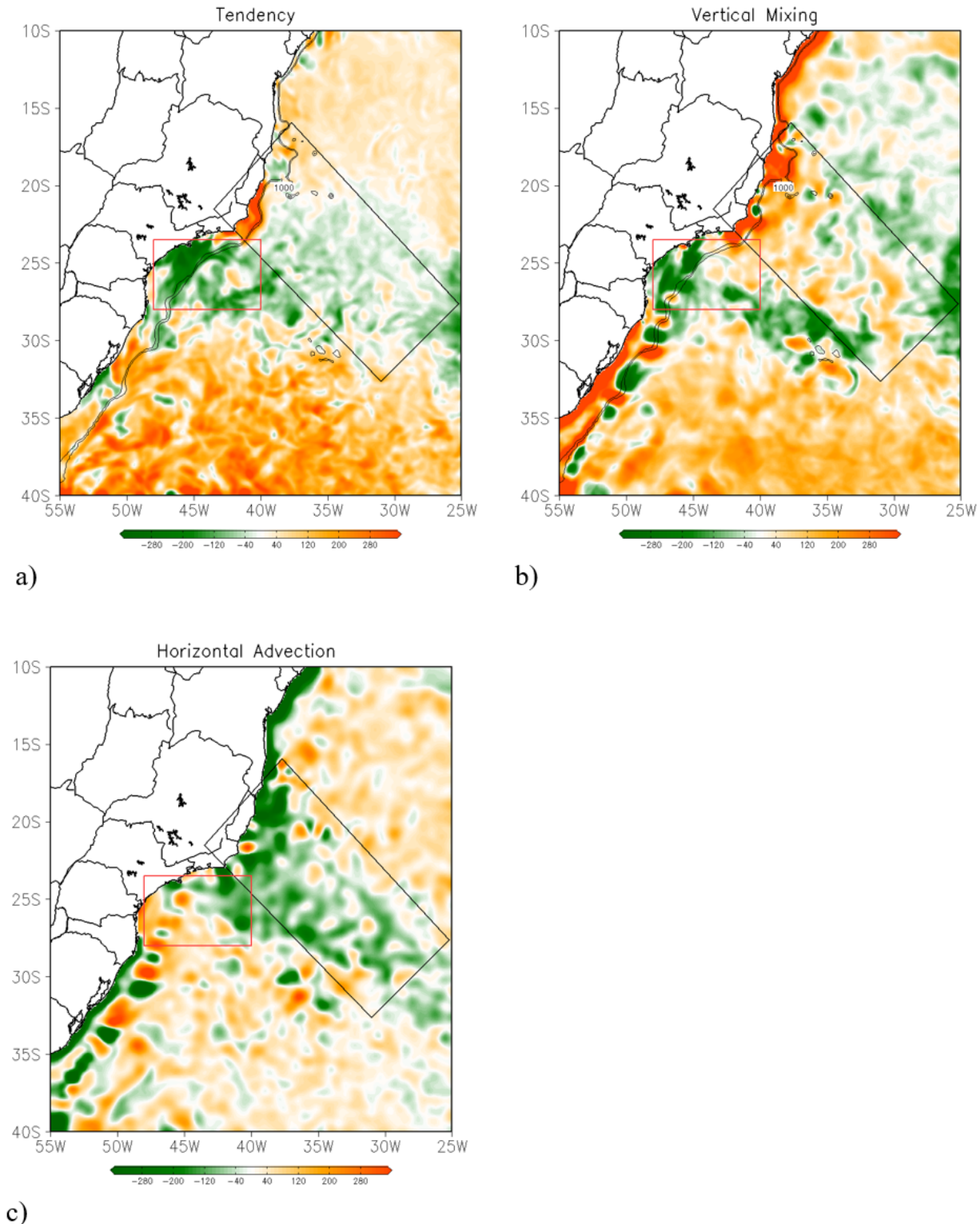


**Figure 8**

Heat budget terms of Equation 3, averaged in time for the three SACZ cases, 1 to 3 as indicated in Table 1. (a) Heat storage. (b) Vertical mixing (vertical heat diffusion + vertical heat advection) (c) Horizontal heat advection. All terms are integrated from surface down to the mixed layer depth ( $-h$ ) and multiplied by  $\rho C_p$ . The panels in this figure were obtained from COA2 experiment. All units are in  $\text{W}\cdot\text{m}^{-2}$ .

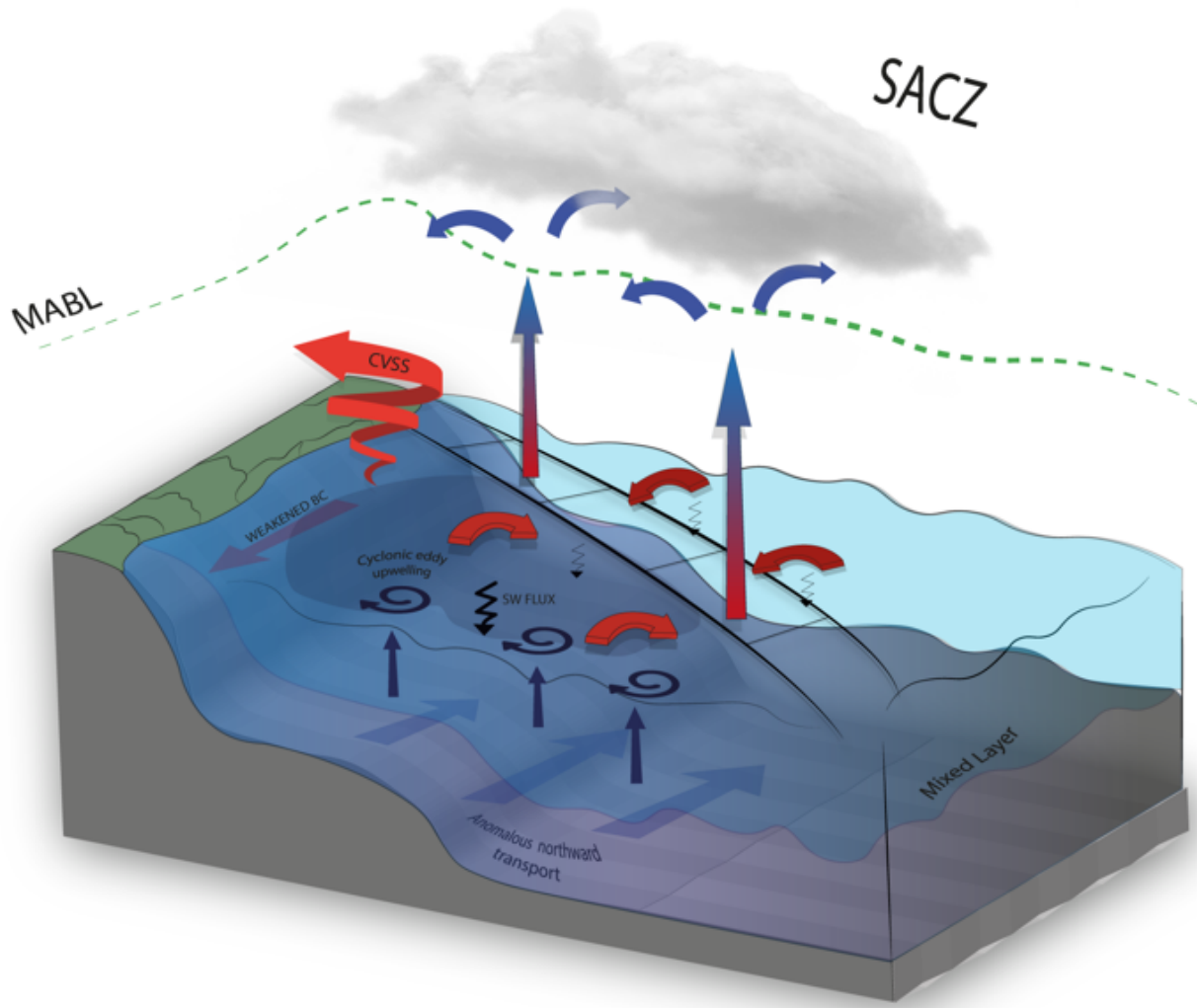


**Figure 9**

Schematic representation of Oceanic SACZ processes, showing the ocean dynamic and thermodynamic mechanisms that decrease the SST, which is represented by the darker blue area. The convergence of surface winds and divergence aloft (curved red arrows around dashed green line) causes the weakening of the Brazil Current (BC) (represented by the thicker darker red arrow parallel to the continent) and consequently decreasing the heat transport towards to the south, likely caused by this weakened current. This generates cold water anomalies, as indicated by dark blue thicker northward blue arrows. This CB's representation should be interpreted as the whole current action which extends far offshore but is not represented in its totality here for the sake of schematic's clarity. Upwelling is caused by well-established dynamic atmospheric circulation and oceanic eddy activity (darker blue spiral). The thermodynamic

mechanism which is a reduction of the shortwave radiation reaching the sea surface is represented by the thick cloud cover presence (gray clouds), which is a remarkable SACZ feature. The presence of a Cyclonic Vortex Southwest of SACZ (CVSS) is represented by the thicker curved red arrow.

## Supplementary Files

This is a list of supplementary files associated with this preprint. Click to download.

- [SUPPLEMENTARYMATERIAL.docx](#)